Available online at www.sciencedirect.com

ScienceDirect

Geochimica et Cosmochimica Acta 328 (2022) 1–18

Geochimica et Cosmochimica Acta

www.elsevier.com/locate/gca

Early diagenetic constraints on Permian seawater chemistry from the Capitan Reef

Roger N. Bryant [a,*], Theodore M. Present [b], Anne-Sofie C. Ahm [c,d], Harry-Luke O. McClelland [e], Dan Razionale [a], Clara L. Blättler [a]

[a] Department of the Geophysical Sciences, The University of Chicago, 5734 S. Ellis Ave, Chicago, IL 60637, USA
[b] Division of Geological and Planetary Sciences, California Institute of Technology, 1200 E California Blvd, Pasadena, CA 91125, USA
[c] Department of Geosciences, Princeton University, Guyot Hall, Princeton, NJ 08544, USA
[d] School of Earth & Ocean Sciences, Bob Wright Centre A405, University of Victoria, Victoria, BC V8W 2Y2, Canada
[e] School of Geography, Earth and Atmospheric Sciences, University of Melbourne, Grattan Street, Parkville, Victoria 3010, Australia

Received 3 September 2021; accepted in revised form 25 April 2022; Available online 30 April 2022

Abstract

The Capitan Reef Complex in West Texas is famous for its high prevalence of early marine cements, unusual for a Phanerozoic platform, leading some to suggest that Precambrian styles of carbonate sedimentation enjoyed a Permian encore. Here, we use patterns of stable Ca, Mg, C and S isotopes to better understand the environmental driver(s) of the enigmatic cementation. We find that calcite that is the most enriched in ^{44}Ca has $\delta^{34}S$ values that approach the inferred composition of Permian seawater sulfate. Microbial sulfate reduction in pore fluids must have been spatially and temporally coincident with recrystallization of primary carbonate phases, such that substantial ^{34}S-enriched sulfate was incorporated into diagenetic calcite under relatively closed-system conditions. Moreover, the magnitude of ^{34}S-enrichment of carbonates relative to seawater was strongly influenced by local diagenetic conditions, with fluid-buffered early marine cements, shelf, reef, and upper slope preserving more seawater-like S isotope ratios than the more sediment-buffered lower slope. Some samples are far more ^{34}S-enriched relative to seawater than those from modern sites in similar depositional environments, possibly responding to specific combinations of sedimentary parameters (e.g., grain size, porosity, organic matter rain rate). Additionally, the sulfate concentration in the Delaware Basin might have been slightly lower than modern levels, leading to more extensive isotopic evolution of sulfate in pore waters during carbonate recrystallization. Based on the data and a numerical model of carbonate recrystallization, we suggest that one driver of the extensive seafloor cement precipitation in the Capitan Reef Complex was a Permian water column $[Ca^{2+}]$:$[SO_4^{2-}]$ ratio somewhere between 1 and modern seawater.

Keywords: Carbonate diagenesis; Ca isotopes; Mg isotopes; S isotopes; Sulfate reduction

1. INTRODUCTION

Our knowledge of the history of Earth's surface oxidation state owes much to measurements of the sulfur isotope composition ($\delta^{34}S$) of sulfur-bearing phases in marine sedimentary rocks (Garrels and Lerman, 1981; Berner, 1989; Canfield, 2001; Canfield and Farquhar, 2009). Rock-derived $\delta^{34}S_{sulfate}$ values approximate seawater

* Corresponding author.
E-mail addresses: rnbryant@uchicago.edu (R.N. Bryant), tpresent@caltech.edu (T.M. Present), annesofieahm@uvic.ca (A.-S.C. Ahm), hmcclelland@unimelb.edu.au (H.-L.O. McClelland), drazionale@uchicago.edu (D. Razionale), cblattler@uchicago.edu (C.L. Blättler).

https://doi.org/10.1016/j.gca.2022.04.027
0016-7037/

$\delta^{34}S_{sulfate}$ (Claypool et al., 1980; Paytan et al., 1998; Kampschulte and Strauss, 2004; Rennie et al., 2018), while rock-derived $\delta^{34}S_{sulfide}$ values record the signal of microbial sulfate reduction, which discriminates against the heavy isotope, ^{34}S (Leavitt et al., 2013; Fike et al., 2015). The magnitude of isotopic offsets between coeval $\delta^{34}S_{sulfate}$ and $\delta^{34}S_{sulfide}$ values (Δ_{pyr}) have long been thought to reflect the relative magnitude of global burial fluxes of oxidized (i.e., sulfates) vs. reduced sulfur (i.e., sulfides) (Canfield and Teske, 1996; Fike et al., 2006). Together, time-calibrated records of $\delta^{34}S_{sulfate}$ and Δ_{pyr} offer the potential for semi-quantitative assessment of $[SO_4^{2-}]_{seawater}$ using simple steady state models that relate the rate of change of rock-derived $\delta^{34}S_{sulfate}$ to the size of the global sulfate reservoir (Kah et al., 2004; Planavsky et al., 2012; Algeo et al., 2015). However, whereas seawater $\delta^{34}S_{sulfate}$ is well-constrained through the Mesozoic and Cenozoic Eras by a combination of relatively continuous marine barite (Paytan et al., 1998; Paytan, 2004), taxon-specific carbonate-associated sulfate (CAS) (Burdett et al., 1989; Rennie et al., 2018), and episodic massive sulfate evaporites (Claypool et al., 1980), the Paleozoic and Precambrian seawater $\delta^{34}S_{sulfate}$ record is comparatively patchy and uncertain (Fike et al., 2015). The patchiness is due to the subduction of most pre-Jurassic oceanic crust (and deep-sea sediments hosting barite and pelagic fossils). The uncertainty in the seawater $\delta^{34}S_{sulfate}$ record is due to 'noise' in the most temporally continuous and ubiquitous seawater $\delta^{34}S_{sulfate}$ record, bulk-rock CAS (Present et al., 2020).

Recent work has shown that the 'noise' in the bulk-rock $\delta^{34}S_{CAS}$ record, which might superficially be interpreted as rapid oscillations in seawater $\delta^{34}S_{sulfate}$, is likely largely due to bulk-rock CAS being an inconsistent recorder of seawater $\delta^{34}S_{sulfate}$. Firstly, stratigraphic bulk-rock $\delta^{34}S_{CAS}$ variability can, in some cases, be attributed to depositional environment or diagenetic conditions (Richardson et al., 2019a; Murray et al., 2021). Secondly, coeval carbonates from different depositional settings record markedly different bulk-rock $\delta^{34}S_{CAS}$ values (Present et al., 2019), despite the presumed homogeneity of seawater $\delta^{34}S_{sulfate}$. Thirdly, different minerals (e.g., dolomite vs. calcite) and components in carbonate rocks (e.g., bioclasts vs. different types of cement) can preserve wildly different $\delta^{34}S_{CAS}$ values (Present et al., 2015; Present et al., 2019) and CAS concentrations (Present et al., 2015; Richardson et al., 2019b; Rose et al., 2019), responding to their local conditions of formation and diagenesis. Finally, the 'noise' in bulk-rock $\delta^{34}S_{CAS}$ data increases with sample age, implying that post-depositional processes (i.e., early and late diagenesis) can affect bulk-rock $\delta^{34}S_{CAS}$ (Present et al., 2020). More promisingly, other studies have found that primary $\delta^{34}S_{CAS}$ values can be preserved through burial diagenesis and hydrothermal dolomitization (Fichtner et al., 2017; Schurr et al., 2021). In summary, the degree to which bulk-rock $\delta^{34}S_{CAS}$ records seawater $\delta^{34}S_{sulfate}$ therefore is highly dependent on carbonates' environment of deposition, mineralogy, component make-up, and post-depositional history.

To increase the utility of the existing bulk-rock $\delta^{34}S_{CAS}$ record, it would be beneficial to have a unifying geochemical framework for understanding the diagenetic controls on bulk-rock $\delta^{34}S_{CAS}$. Ideally, different diagenetic endmembers (pristine and altered) would purposely be sampled to map out the entire phase space. The advantage of such an approach is that it can be applied systematically at the bulk-rock level without detailed facies/sequence stratigraphic context or the presence of specific carbonate components (e.g., bioclasts), both of which are absent and/or underconstrained through much of the carbonate record. Here, using diagenetically altered carbonates, we show that combined bulk-rock $\delta^{34}S_{CAS}$ values with magnesium ($\delta^{26}Mg$) and calcium ($\delta^{44/40}Ca$) isotope ratios, in addition to minor/major element ratios (e.g., Sr/Ca, Mn/Ca, Fe/Ca), provide a powerful geochemical toolkit for understanding marine carbonate diagenesis. These systems together distinguish between restricted basinal (i.e., evaporitic) and open-ocean depositional settings (Blättler et al., 2018; Higgins et al., 2018), which affect the degree to which $\delta^{34}S_{CAS}$ resembles seawater $\delta^{34}S_{sulfate}$ (Fike et al., 2015). They are also sensitive to the nuances of carbonate recrystallization and closed vs. open system behaviour during early marine diagenesis (Blättler et al., 2015; Ahm et al., 2018; Higgins et al., 2018; Ahm et al., 2019; Jones et al., 2020; Staudigel et al., 2021; Crockford et al., 2021), and are therefore a function of local depositional and diagenetic conditions – another major control on $\delta^{34}S_{CAS}$ (Richardson et al., 2019a; Murray et al., 2021) – and the chemical composition of the overlying water column.

To test whether $\delta^{26}Mg$ and/or $\delta^{44/40}Ca$ can be useful for quantitatively predicting how well $\delta^{34}S_{CAS}$ resembles seawater $\delta^{34}S_{sulfate}$, we apply these analyses to the micro-drilled, late Guadalupian-age Capitan Reef Complex samples of (Present et al., 2019), for which $\delta^{34}S_{CAS}$, overlying seawater $\delta^{34}S_{sulfate}$, depositional facies, petrographic context, other geochemical indices ($\delta^{13}C_{carb}$, $\delta^{18}O$), and mineralogy are already well-constrained. We characterize the relationships among samples with different depositional and diagenetic histories and assess the mechanisms and conditions that generate these relationships. Here, we also adapt an existing diagenetic model (Ahm et al., 2018), to explore how established diagenetic indices can be used to disentangle diagenetic effects on $\delta^{34}S_{CAS}$, constrain Permian seawater chemistry, and potentially explain anomalous features of the Capitan Reef Complex such as the abundant and ubiquitous early marine cements that are reminiscent of Precambrian carbonates (Grotzinger and Knoll, 1995). Moving forward, correlations between any mineral- or texture-specific suite of $\delta^{34}S_{CAS}$ values and $\delta^{26}Mg$ and/or $\delta^{44/40}Ca$ form a basis for assessing the degree to which $\delta^{34}S_{CAS}$ measurements in other, less well studied locations capture contemporaneous seawater $\delta^{34}S_{sulfate}$. This information could be used to screen the bulk-rock $\delta^{34}S_{CAS}$ record through Earth history for samples whose $\delta^{34}S_{CAS}$ values have been altered by diagenesis and do not reflect seawater $\delta^{34}S_{sulfate}$.

2. MATERIALS & METHODS

2.1. Isotopic notation

For the purposes of this study, we use delta notation to describe the deviation in per mil (‰) of the isotopic

composition of samples from known reference standards (Coplen, 2011). For sulfur isotopes, $\delta^{34}S_{sample} = [(^{34}S/^{32}S)_{sample}/(^{34}S/^{32}S)_{V\text{-}CDT}] - 1$, where V-CDT is the Vienna Canyon Diablo Troilite reference standard (Ding et al., 1999). For carbon isotopes, $\delta^{13}C_{sample} = [(^{13}C/^{12}C)_{sample}/(^{13}C/^{12}C)_{V\text{-}PDB}] - 1$, where V-PDB is the Vienna-Pee Dee Belemnite reference standard. For oxygen isotopes, $\delta^{18}O_{sample} = [(^{18}O/^{16}O)_{sample}/(^{18}O/^{16}O)_{V\text{-}PDB}] - 1$. For magnesium isotopes, $\delta^{26}Mg_{sample} = [(^{26}Mg/^{24}Mg)_{sample}/(^{26}Mg/^{24}Mg)_{DSM3}] - 1$, where DSM3 is the Dead Sea Magnesium reference standard (Galy et al., 2003). For calcium isotopes, $\delta^{44/40}Ca_{sample} = [(^{44}Ca/^{40}Ca)_{sample}/(^{44}Ca/^{40}Ca)_{SW}] - 1$, where SW is IAPSO modern seawater (Hippler et al., 2003). For reference, IAPSO is +1.86‰ relative to NIST915a (Jochum et al., 2005), the other most used Ca reference standard.

2.2. Samples

The sample set for this study features carbonates from the late Guadalupian-age Capitan Reef Complex in the Permian Basin of West Texas and New Mexico, one of the best preserved and best studied ancient mixed siliciclastic and carbonate platform and slope systems. Depositional facies from shelf to basin are correlated by detailed biostratigraphy and sequence stratigraphic models (Silver and Todd, 1969; Tyrrell Jr, 1969; Borer and Harris, 1991; Osleger, 1998; Kerans and Tinker, 1999; Sarg et al., 1999; Wilde et al., 1999; Lambert, 2002; Rush and Kerans, 2010), crucially allowing carbonates deposited from the same water column but in different depositional environments to be compared. The carbonates record a range of early-late diagenetic processes in their petrographic and geochemical characteristics (Mazzullo and Cys, 1977; Schmidt, 1977; Yurewicz, 1977; Given and Lohmann, 1986; Garber et al., 1989; Mruk, 1989; Scholle et al., 1992; Mutti and Simo, 1994; Mazzullo, 1999; Melim and Scholle, 2002; Budd et al., 2013; Frost et al., 2013; Bishop et al., 2014; Wu et al., 2020). Notably, syn- and eogenetic marine diagenetic processes dominated the texture of Capitan Reef Complex limestones and dolomites. Primary fibrous, bladed, isopachous, and micritic cements comprise most of the rock volume of reef and fore-reef (Cys et al., 1977; Mazzullo and Cys, 1977; Grotzinger and Knoll, 1995), and voluminous precipitates form allochems and void-filling cements in peritidal shelf-top strata (Kendall, 1969; Esteban and Pray, 1977; Assereto and Kendall, 1977; Esteban and Pray, 1983; Chafetz et al., 2008). Stratal geometries of dolomite show that platform interior-derived brines drove dolomite replacement of precursor aragonitic and calcitic sediments in concert with syndepositional accommodation cycles (Adams and Rhodes, 1960; Kendall, 1969; Mutti and Simo, 1994; Melim and Scholle, 2002; Koša and Hunt, 2006; Garcia-Fresca et al., 2012). Neomorphic dolomite textures include fabric-retentive mimetic dolomite and fabric-selective non-mimetic dolomite (Mutti and Simo, 1993; Mutti and Simo, 1994; Melim and Scholle, 2002; Frost et al., 2013), and primary aragonite cements were replaced by neomorphic calcite (Mazzullo, 1980; Chafetz et al., 2008). Later generations of percolating fluids caused coarser dolomite crystallization along permeable sandstones (Melim and Scholle, 1989), Neptunian fracture systems, and eogenetically fractured tepee and sheet crack structures (Kendall, 1969; Melim and Scholle, 1989; Koša and Hunt, 2006; Budd et al., 2013; Frost et al., 2013). Rock fabric was largely unchanged during burial diagenesis, although porosity was modified by anhydrite and calcite cement precipitation and dissolution (Schmidt, 1977; Garber et al., 1989; Mruk, 1989; Scholle et al., 1992; Budd et al., 2013; Loyd et al., 2013; Frost et al., 2013).

Contemporaneous seawater $\delta^{34}S_{sulfate}$ value is constrained to ~8–10‰ VCDT by the composition of local and more remote mid-late Permian-age evaporite deposits (Thode et al., 1961; Holser and Kaplan, 1966; Claypool et al., 1980; Sarg, 1981; Hill, 1990; Leslie et al., 1997; Kirkland et al., 2000; Present et al., 2020). Present et al. (2019) collected carbonate hand-samples along a shelf-basin transect through the Yates, Tansill, Capitan and Bell Canyon formations (Fig. 1A) in McKittrick Canyon, Guadalupe Mountains, National Park, Texas, and sub-sampled specific textures/phases (e.g., different generations of cement, or minerals; Fig. 1B-C) using a handheld rotary micro-drill. For this study, we micro-drilled 259 ~ 1–3 mg sub-samples from the same spots already sub-sampled by (Present et al., 2019), based on the assumption that the newly sampled material would be chemically and mineralogically equivalent.

2.3. Standards

To correct our isotopic data to international reference standards, we processed various isotopic reference materials along with our samples. For Ca isotopes, these were: seawater (collected at Woods Hole Oceanographic Institution), EN-1 from the USGS (modern *Tridacna* shell, Enewetak lagoon, Marshall Islands), NIST SRM 915b calcium carbonate, the 'PUA' in-house aragonite standard from Princeton University, and an in-house aragonite standard (San Salvador Sand; 'SSS'). For Mg isotopes, these were: seawater, the 'RUB' in-house calcite standard from Ruhr University Bochum (Riechelmann et al., 2018), a high purity Mg ICP standard obtained from Princeton University, and an in-house dolomite standard from the University of Chicago collection ('IHD').

2.4. Wet chemistry and ion chromatography (Dionex)

For each carbonate sample or standard, 1 mg was added to 1 mL of a 0.1 M acetic acid, 0.05 M ammonium hydroxide solution and treated ultrasonically for 4–8 hours to ensure complete dissolution of carbonate materials. For carbonate samples, aliquots of solution were diluted using the same acetic acid/ammonium hydroxide solution to generate solutions with $[Ca^{2+}]$ of 100–200 ppm or $[Mg^{2+}]$ of 10–25 ppm. Sample aliquots of 25 μL were then autosampled and processed with a Thermo/Dionex ion chromatography system, using 30 mM methanesulfonic acid as the eluent (25 mM for seawater). To minimize cross-contamination between sample vials and fraction collection vials, we 'chased' the sample injection with a 25 μL injection

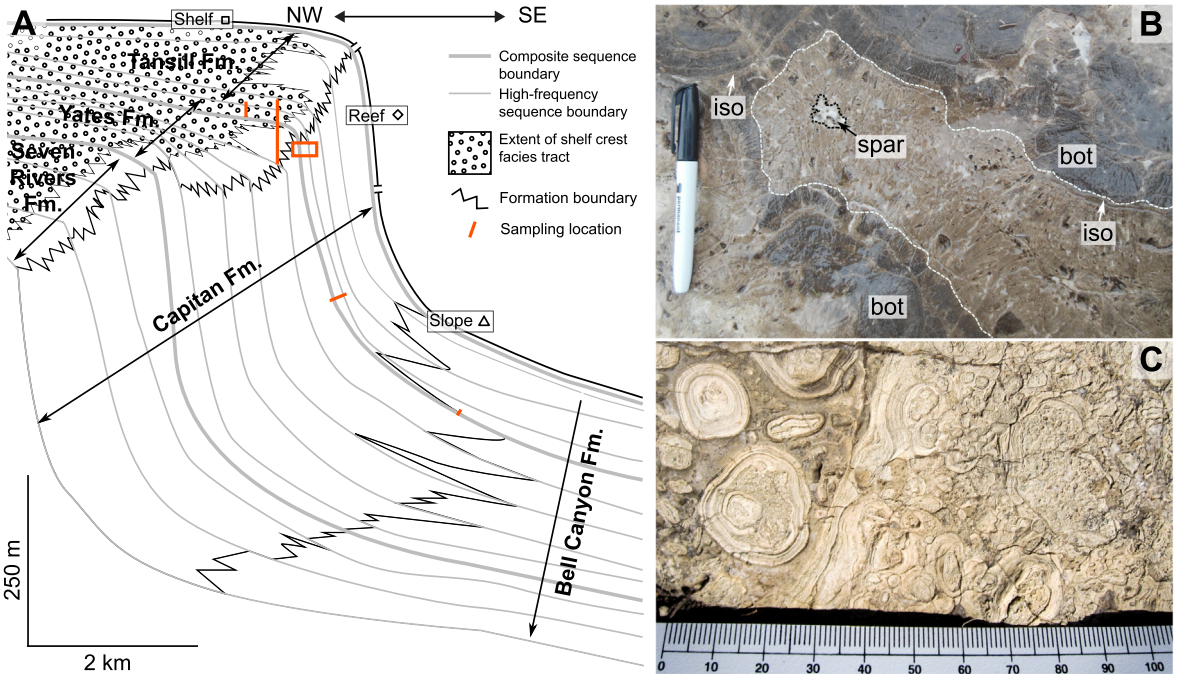

Fig. 1. (A) Stratigraphy of Guadalupian-age strata of the Capitan Reef Complex in west Texas, after Present et al. (2019), and references therein. Sampling locations of Present et al. are marked in orange. Samples were taken along a single composite sequence boundary so that samples would be roughly age equivalent. Marked above the uppermost composite sequence boundary are the approximate extents of the shelf, reef, and slope facies tracts, along with the symbols used to represent them in subsequent figures. (B) Different generations of carbonate cement (e.g., botryoids – 'bot', isopachous cements – 'iso', spar) in the Capitan Reef. The dashed white line marks the boundary between the botryoidal cements and later generations of infilling cement, including spar (ringed by the dashed black line). (C) Mimetically dolomitized pisoid rudstone, from the shelf facies tract – scale bar is in mm.

of ultrapure water, designed to clean the autosampler needle and tubing prior to in-line fraction collection (Razionale et al., 2021). Ca and Mg were then isolated from samples by collecting the eluent in timed windows. Ca and Mg peak areas were used to calculate molar Mg/(Ca + Mg) ratios.

Ca and Mg solutions were transferred to Teflon vials and dried down on a hotplate at ~150 °C; samples were then treated with 200 µL 20 N nitric acid for ~30 minutes to oxidize and volatilize any organic compounds and dried down again. After using the Ca or Mg peak areas as assessed by the in-line conductivity detector during ion chromatography to calculate the mass of Ca or Mg in each vial, the appropriate volume of 2% nitric acid was added to each vial to standardize the [Ca] or [Mg] of each sample to ~1 ppm and ~150 ppb, respectively.

2.5. Multi-collector mass spectrometry methods

Ca and Mg isotope ratios were measured using a Thermo Neptune XT multi-collector inductively-coupled plasma mass spectrometer (MC-ICP-MS). For Ca isotope ($\delta^{44/42}$Ca) analyses, samples were introduced using an ESI Apex-Ω desolvating nebulizer. Sample-standard bracketing was used to correct for instrumental mass fractionation. Medium- or high-resolution modes were used to avoid interferences such as $ArHH^+$ and to allow stable measurement of the low-mass shoulder over > 12-hour-long runs. For all sample/standard measurements, we used a Faraday cup at 43.5 amu to monitor $^{87}Sr^{++}$ and corrected for Sr by assuming that the contributions of $^{84}Sr^{++}$, $^{86}Sr^{++}$ and $^{88}Sr^{++}$ to ^{42}Ca, ^{43}Ca, and ^{44}Ca are related to $^{87}Sr^{++}$ by their natural abundances. The effect of [Ca] on $\delta^{44/42}$Ca was established using a 5-point calibration between 0.9 and 1.1 ppm and corrected for using the ratio of the intensity of the mass 44 ion beam for each sample to that of the prior analysis of the bracketing standard, whose [Ca] was known and constant throughout the run. $\delta^{44/40}$Ca values were calculated from $\delta^{44/42}$Ca using established kinetic fractionation laws (Young et al., 2002) and assuming no radiogenic ^{40}Ca excess. Long-term external reproducibility was ± 0.12‰ (2σ, n = 44) for NIST SRM 915b, which had an average $\delta^{44/40}$Ca of −1.12‰ (Razionale et al., 2021), in line with published values.

For Mg isotope analyses, samples were introduced using a dual-path glass cyclonic spray chamber and sample-standard bracketing was used to correct for instrumental mass fractionation. Due to the absence of significant isobaric interferences at masses 24, 25 and 26, low resolution mode was used. The effect of [Mg] on δ^{26}Mg was established using a 5-point calibration between 135 and 165 ppb, and corrected for using the ratio of the intensity of mass 24 for each sample to that of the prior analysis of the bracketing standard, whose [Mg] was known and constant throughout the run. Long-term external reproducibility was ± 0.10‰ (2σ, n = 34) for IHD, ±0.11‰

(2σ, n = 44) for seawater, and ± 0.11‰ (2σ, n = 30) for RUB, which had average δ^{26}Mg values of −1.77‰, −0.78‰, and −3.69‰, respectively, the latter two in line with published values (Riechelmann et al., 2018).

For both Ca and Mg, we used triple-isotope plots to ensure the mass-dependence of all measured raw data (see Table S1 for raw isotope data).

2.6. Quadrupole ICP-MS methods

A suite of major and trace element abundances was measured using a Thermo Scientific iCAP RQ ICP-MS. Kinetic energy discrimination (KED) mode, which employs He gas and limits polyatomic interferences, was used to measure Fe, whereas standard (STD) mode was used to measure Ca. Sr and Mn were analyzed in both STD and KED mode. Samples and standards were adjusted to 10 ppm Ca in 2% nitric acid prior to analysis to mitigate matrix related effects. Additionally, samples were spiked with equal amounts of an internal standard solution containing Sc, In, and Y to correct for instrumental drift during analysis. A five-point calibration curve was generated for each element at the start of each run and used to calculate elemental concentrations. One calibration standard and the calibration blank were analyzed intermittently throughout each run for quality control, in addition to one duplicate sample analysis every 15 samples. Data are reported as molar ratios to Ca + Mg.

2.7. Numerical model

Sulfate was added to a previously-published numerical model simulating early marine diagenesis of shallow water carbonates along a one-dimensional advective flow path (Ahm et al., 2018). The model consists of a prescribed series of boxes numbered from 1 (closest to the water column) to 'n' (farthest along the flow path). Fluid flow is assumed to occur by advection rather than diffusion, based on evidence that fluid flow in the Capitan Formation was density driven (Melim and Scholle, 2002). Advection and recrystallization occur at a constant rate until 100% of the primary mineral (e.g., aragonite) has been converted to diagenetic mineral (e.g., calcite). The eventual chemical compositions of diagenetic minerals vary between box 1 and 'n' because the fluid becomes progressively more chemically evolved by all chemical reactions further along the flow path. Thus, the chemistry of diagenetic minerals in box 1 can be described as more fluid-buffered (i.e., determined by the chemistry of the infiltrating fluid, in this case seawater) and the chemistry of diagenetic minerals in box 'n' can be described as more sediment-buffered (i.e., determined by the chemistry of the recrystallizing primary mineral plus any other reactions happening in pore waters). Sulfate is supplied by advection and primary mineral dissolution and then is lost from the fluid components of the system by incorporation into diagenetic mineral (as CAS) and at a constant rate via microbial sulfate reduction (MSR) – i.e., organic matter is assumed to be present in non-limiting amounts. We assumed that all sulfide was immediately lost from the system as pyrite. Parameters for the model were derived from a combination of published experimental data, including distribution coefficients and fractionation factors between aqueous sulfate and aragonite- and calcite-bound CAS (Barkan et al., 2020). Initial conditions (seawater chemistry) and rates of recrystallization and MSR were varied to generate the best visual fit between model and data. A list of all key assumptions made is given in Table 1.

We conducted a sensitivity analysis to explore the model response (particularly the differences between the $\delta^{44/40}$Ca and $\delta^{34}S_{CAS}$ values of fluid- and sediment-buffered diagenetic calcite) to a range of inputs, including initial mineralogy (aragonite vs. high-Mg calcite), $[SO_4^{2-}]_{seawater}$, $[Ca^{2+}]_{seawater}$, MSR rate, and the Ca isotopic fractionation factor of recrystallization (see Discussion below and supplementary material for more details).

3. RESULTS

A total of 249 sub-samples were analyzed. These samples had Mg/(Ca + Mg) ratios (mol/mol) ranging from 0.003 (low-Mg calcite) to 0.5 (pure dolomite). Present et al. (2019) used a combination of field relationships and petrography to map all hand samples and subsamples onto the detailed facies framework for the Capitan Reef (Tinker, 1998). Here we use a simplified version of that facies framework plus Mg/(Ca + Mg) (this study) as context for comparisons between δ^{13}C, δ^{18}O, and $\delta^{34}S_{CAS}$ (Present et al., 2019), and $\delta^{44/40}$Ca and δ^{26}Mg (this study). Generally, all samples can be assigned to either early marine cements (EMC, i.e., originally-aragonitic botryoids or isopachous cements; Fig. 1B), later diagenetic sparry cements (i.e., equant or poikilitic calcite), or to sedimentary textures from the shelf, reef, or slope facies tracts (Fig. 1A). Shelf samples came from supratidal barrier island/tepee-pisolite, shoreface, shoal, and outer shelf shallow subtidal depositional environments of the Yates and Tansill formations; inner shelf evaporitic lagoonal facies were not sampled. Reef samples came from a shelf margin (but not raised barrier) reef in a deep subtidal—possibly mesophotic—reef of the Capitan Formation. Slope samples of the Capitan and Bell Canyon formations were forereef carbonate debrites and turbidites shed from the reef, which interfingered with basinal clastics. Dolomitization in the shelf, reef, and forereef/slope was dominantly fabric-retentive with subordinate fabric-destructive recrystallization, including mimetic replacement of aragonite marine cements and fossils (Melim and Scholle, 2002; Frost et al., 2013).

3.1. Magnesium isotopes

Measured δ^{26}Mg values range from −3.41 to −1.41‰ (Table S1). Generally, samples that are classified as low-Mg calcite [Mg/(Ca + Mg) < 0.04] have more negative and variable δ^{26}Mg values [avg. = −2.75 ± 0.34‰ (1σ, n = 73)], whereas samples with Mg/(Ca + Mg) > 0.04 (variable mixtures of dolomite and calcite) have more positive and less variable δ^{26}Mg values [avg. = −1.88 ± 0.21‰ (1σ, n = 162)]. When plotted against Mg/(Ca + Mg), δ^{26}Mg values monotonically increase, plateauing at high Mg concentrations (Fig. 2).

Table 1
List of key model input parameters and literature justification.

Parameter	Value(s)	Reference
u (advection rate)	0.1 m y^{-1}	(Henderson et al., 1999)
MSR rate constant	3e−3 y^{-1}	(Canfield, 1991) and refs. therein; this study.
Recrystallization rate constant	5e−6 y^{-1}	(Higgins et al., 2018; Staudigel et al., 2021)
$[Mg^{2+}]_{seawater}$	45 mM	(Farkaš et al., 2007)
$[Ca^{2+}]_{seawater}$	13 mM	(Farkaš et al., 2007)
$[DIC]_{seawater}$	3 mM	(Farkaš et al., 2007)
$[SO_4^{2-}]_{seawater}$	13 to 20 mM	$[SO_4^{2-}]$ in excess relative to $[Ca^{2+}]$; (Horita et al., 2002)
$\delta^{26}Mg_{seawater}$	−0.3 to −0.1‰	This study.
$\delta^{44/40}Ca_{seawater}$	−0.4 to −0.2‰	This study.
$\delta^{13}C_{fluid}$	−2‰	This study.
$\delta^{34}S_{seawater}$	+8 to 10‰	(Present et al., 2019) and refs. therein.
$\varepsilon^{26}Mg_{aq\text{-}cc}$	−2.58‰	(Li et al., 2015)
$\varepsilon^{26}Mg_{aq\text{-}arag}$	−1.15‰	(Wang et al., 2013)
$\varepsilon^{26}Mg_{aq\text{-}dol}$	−2 to −1.81‰	(Li et al., 2012; Higgins et al., 2018)
$\varepsilon^{44/40}Ca_{aq\text{-}arag}$ (primary)	−1.6‰	(Higgins et al., 2018)
$\varepsilon^{44/40}Ca_{aq\text{-}calc}$ (primary)	−1.0‰	(Gussone et al., 2005)
$\varepsilon^{44/40}Ca_{aq\text{-}calc}$ (diagenetic/ recrystallization)	0 to −0.5‰	(Fantle and DePaolo, 2007; Bradbury and Turchyn, 2018; Mills et al., 2021)
$\varepsilon^{34}S_{SO4\text{-}CAS(cc)}$	+1.7‰	(Barkan et al., 2020)
$\varepsilon^{34}S_{SO4\text{-}CAS(arag)}$	+1.0‰	(Barkan et al., 2020)
$\varepsilon^{34}S_{SO4\text{-}CAS(dol)}$	0‰	Similarity between dolomite and evaporite $\delta^{34}S$ (Present et al., 2019)
$Kd_{CAS(cc)}$ (partition coeff.)	16e−6	(Barkan et al., 2020)
$Kd_{CAS(arag)}$	8e−6	(Barkan et al., 2020)
$\varepsilon_{SO4\text{-}H2S}$	70‰	(Eldridge et al., 2016)

3.2. Calcium isotopes

Measured $\delta^{44/40}Ca$ values range from −1.73 to −0.46‰ (Table S1; Fig. 3). Samples consisting predominantly of calcite [Mg/(Ca + Mg) < 0.25] have on average slightly more positive $\delta^{44/40}Ca$ values [−0.88 ± 0.19‰ (1 std. dev., n = 133)] than those consisting predominantly of dolomite [−1.02 ± 0.19‰ (1 std. dev., n = 112)]. When $\delta^{44/40}Ca$ values are plotted against $\delta^{26}Mg$ values (Fig. 3), the dolomite-rich samples define a limb with relatively invariant $\delta^{26}Mg$ and more variable $\delta^{44/40}Ca$, whereas low-Mg calcites show substantial variability in both parameters and plot entirely distinctly from dolomites in the Ca-Mg phase space. Samples with 0.04 < Mg/(Ca + Mg) < 0.25 generally fall between the calcites with more positive $\delta^{26}Mg$ and $\delta^{44/40}Ca$ values and the center of the dolomite cluster.

3.3. Major/minor element ratios

Measured Sr/(Ca + Mg), Mn/(Ca + Mg) and Fe/(Ca + Mg) ratios range from 2.3×10^{-6} to 6.6×10^{-4}, 4.1×10^{-7} to 1.3×10^{-3}, and 0 to 5.9×10^{-3} mol mol^{-1}, respectively (n = 248; Table S1; Fig. 4). Samples that are predominantly calcite [Mg/(Ca + Mg) < 0.25] have on average higher and more variable Sr/(Ca + Mg) ratios [$1.7 \times 10^{-4} \pm 1.3 \times 10^{-4}$ mol mol^{-1} (1σ, n = 135)] than samples that are predominantly dolomite [$6.0 \times 10^{-5} \pm 4.1 \times 10^{-5}$ mol mol^{-1} (1σ, n = 113)] (Fig. 4A). Calcite-dominated samples have on average similar Mn/(Ca + Mg) ratios [$1.5 \times 10^{-4} \pm 2.0 \times 10^{-4}$ mol mol^{-1} (1σ, n = 135)] to dolomite-dominated samples [$1.3 \times 10^{-4} \pm 1.7 \times 10^{-4}$ mol mol^{-1} (1σ, n = 113)] (Fig. 4B). Calcite-dominated samples have on average lower Fe/(Ca + Mg) ratios [$1.6 \times 10^{-4} \pm 3.1 \times 10^{-4}$ mol mol^{-1} (1σ, n = 135)] than dolomite-dominated samples [$3.1 \times 10^{-4} \pm 5.8 \times 10^{-4}$ mol mol^{-1} (1σ, n = 113)] (Fig. 4B). Within the calcite-dominated samples, Sr/(Ca + Mg), Mn/(Ca + Mg) and Fe/(Ca + Mg) are highest for a subset of samples from the slope facies tract (specifically, the toe-of-slope) (Fig. 4). The toe-of-slope samples also have more negative $\delta^{44/40}Ca$ values than most of the other calcite-dominated samples (Fig. 4A).

3.4. Comparison of $\delta^{44/40}Ca$ and $\delta^{26}Mg$ with facies, $\delta^{13}C$, $\delta^{18}O$, and $\delta^{34}S_{CAS}$

Sample $\delta^{26}Mg$ values become more negative and more variable along a shelf-basin transect (Fig. 5). This trend is primarily driven by the increasing relative frequency of samples dominated by low-Mg calcite in basinward facies tracts (Fig. 5A). An additional driver of the basinward variability is the fact that dolomite-dominated samples in the slope facies tract are ^{26}Mg-enriched on average relative to dolomite-dominated samples from shelf and reef facies tracts (Fig. 5A). When $\delta^{26}Mg$ values are plotted versus $\delta^{13}C$, $\delta^{18}O$, and $\delta^{34}S_{CAS}$ values (Fig. 5B-D), several commonalities emerge. Dolomite-dominated samples form a tight and distinct cluster in all three plots. Calcite-dominated samples (with the obvious exception of the spar facies tract) generally define a limb of variable $\delta^{26}Mg$ and relatively invariant $\delta^{13}C$, $\delta^{18}O$, and $\delta^{34}S_{CAS}$ in all three plots, with the magnitude of the $\delta^{26}Mg$ deviation from the dolomitic cluster to first order negatively correlating with Mg/(Ca + Mg). Slope and spar facies tracts generally plot farthest from the dolomitic cluster in the $\delta^{13}C$, $\delta^{18}O$, and $\delta^{34}S_{CAS}$ axes.

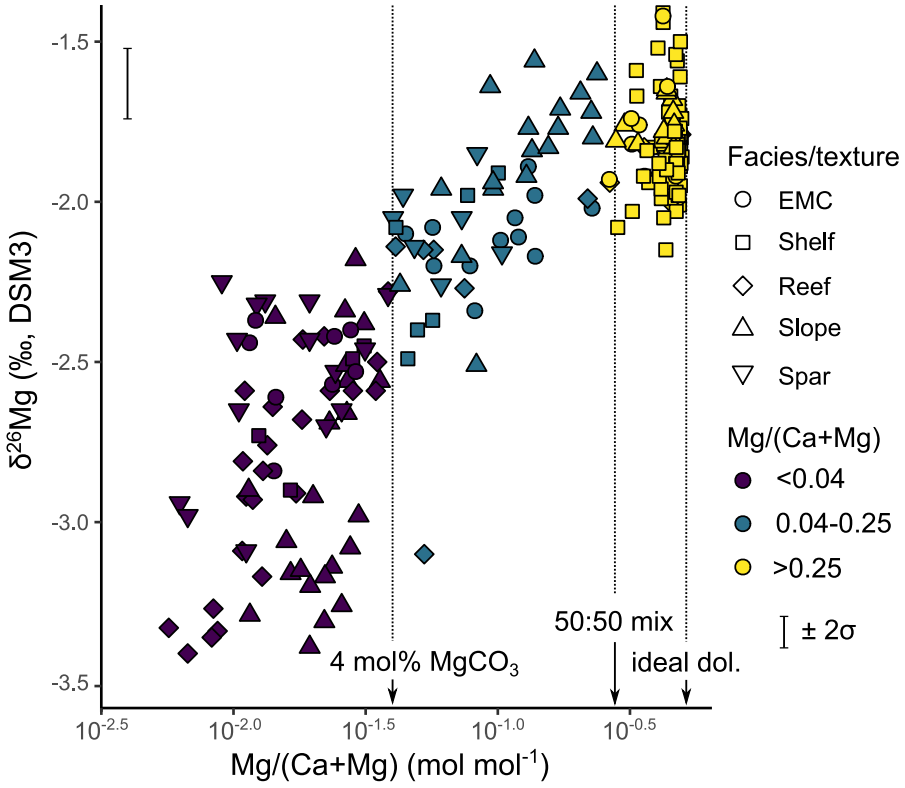

Fig. 2. δ^{26}Mg values for carbonate samples from Capitan Reef, plotted against Mg/(Ca + Mg). Symbols correspond to sample facies/textures and are color coded by Mg/(Ca + Mg). Dashed lines and arrows indicate the x-axis positions of upper limit for Mg in low-Mg calcite, ideal stoichiometric dolomite, and a 50:50 mix of those two mineral end members, respectively.

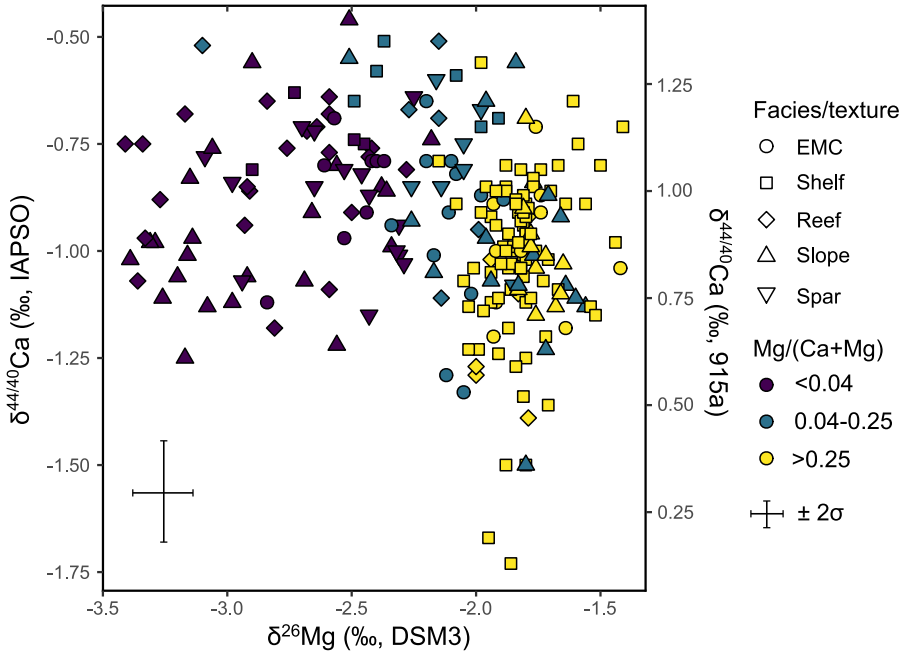

Fig. 3. $\delta^{44/40}$Ca values for carbonate samples from Capitan Reef, plotted against δ^{26}Mg. Symbols correspond to sample facies/textures and are color coded by Mg/(Ca + Mg).

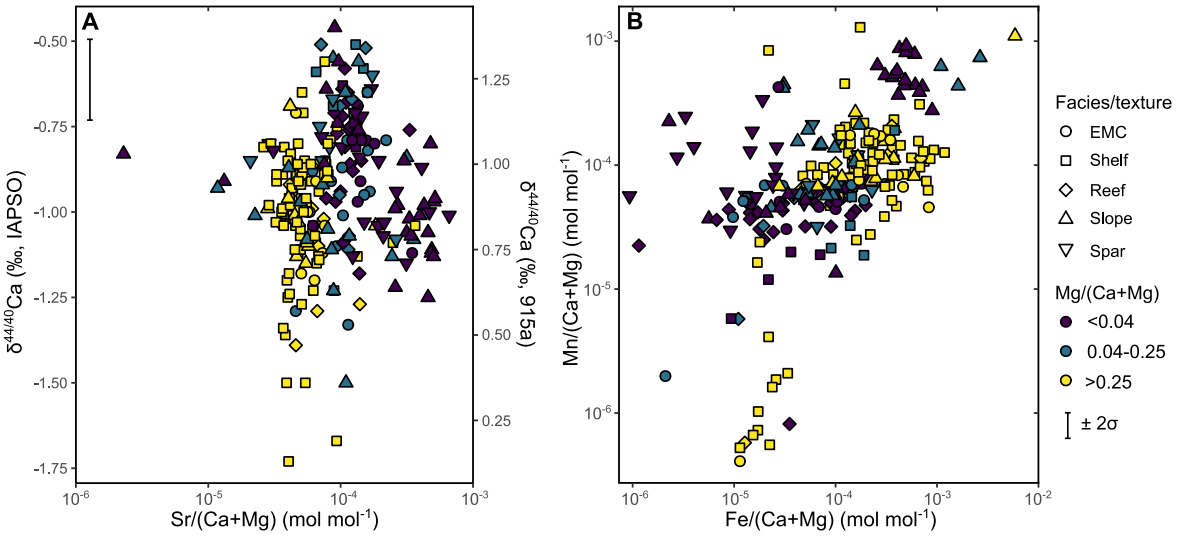

Fig. 4. Minor/major element ratios for carbonate samples from Capitan Reef. (A) Sr/Ca + Mg plotted against $\delta^{44/40}$Ca values, (B) Fe/(Ca + Mg) plotted against Mn/(Ca + Mg). Symbols correspond to sample facies/textures and are color coded by Mg/(Ca + Mg).

Sample $\delta^{44/40}$Ca values show a large degree of variability for both dolomite- and calcite-dominated samples, but calcite-dominated samples are on average enriched in ^{44}Ca relative to dolomite-dominated samples – this is true for all facies tracts where both minerals are present (Fig. 6A). When $\delta^{44/40}$Ca values are plotted against δ^{13}C, δ^{18}O, and $\delta^{34}S_{CAS}$ values (Fig. 6B-D), the data fall into three clusters defined by mineralogy and facies: dolomite-dominated samples, sparry calcite, and non-sparry calcite-dominated samples. When samples with chemistry clearly influenced by meteoric or burial fluids during later diagenesis [i.e., $\delta^{18}O < -2‰$ and negative δ^{13}C; (Present et al., 2019)] are excluded, broad trends are visible between $\delta^{44/40}$Ca and the other variables within the non-sparry calcite-dominated cluster, some of which are clearly defined by the transect from shelf-reef-slope facies tracts. Notably, $\delta^{44/40}$Ca and $\delta^{34}S_{CAS}$ have a significant negative relationship ($R = -0.31$, p-value $= 0.0023$; Fig. S1A), with the most ^{34}S-enriched and ^{44}Ca-depleted samples belonging to the slope facies tract, and the reverse being true for the shelf facies tract. When EMCs are excluded, the correlation between $\delta^{44/40}$Ca and $\delta^{34}S_{CAS}$ becomes clearer ($R = -0.49$, p-value $= 1.3 \times 10^{-5}$; Fig. S1B).

4. INTERPRETATION AND DISCUSSION

The Mg and Ca isotope trends we observe, when coupled with existing geochemical data and facies context (Present et al., 2019), shed new light on the diagenetic histories of the various sedimentary components of the Capitan Reef complex. After interpreting the Mg and Ca isotope data, we will discuss the broader implications for the chemistry of the Delaware Basin and environmental drivers of the precipitation of the early marine cements.

4.1. Magnesium and calcium isotopic constraints on the diagenetic history of the Capitan Reef

We interpret the relationship between samples' δ^{26}Mg values and Mg/(Ca + Mg) (Fig. 2) as indicative of a mixing trend between two isotopically distinct, albeit noisy, end-members: low-Mg calcite and dolomite. While only a minority of samples entirely escaped the pervasive dolomitization of the Capitan Reef Complex, some samples (mostly from the reef and slope facies) are recrystallized calcite – these samples display the most δ^{26}Mg variance. In contrast, the δ^{26}Mg variance in the dolomites is small, which we interpret to mean that dolomite formation was predominantly seawater-buffered with respect to Mg (i.e., only a minor component of the dolomite Mg was sourced from precursor carbonate minerals). Even when [Mg^{2+}] is high, Rayleigh distillation during dolomitization causes the δ^{26}Mg value of the dolomitizing fluid to become progressively more positive (Bialik et al., 2018), so the most negative dolomite δ^{26}Mg value is the most informative regarding the δ^{26}Mg value of the starting fluid. The most negative δ^{26}Mg value of dolomite was ~−2.1‰ and the isotopic fractionation (ε) between aqueous Mg^{2+} and dolomite is −2 to −1.8‰ (Li et al., 2015; Higgins et al., 2018). Our data therefore suggest that the δ^{26}Mg value of the Delaware Basin seawater was between −0.3 and −0.1‰. This is similar to a prior estimate of −0.1‰ by Li et al. (2015), which was based on their experimentally derived dolomite fractionation factor and compiled dolomite δ^{26}Mg values. If calcite formed directly from seawater with a δ^{26}Mg value of −0.3 to −0.1‰ at equilibrium, expected δ^{26}Mg values would be between −2.9 and −2.7‰ (Li et al., 2012; Li et al., 2015), which is broadly consistent with the average δ^{26}Mg value of calcite measured in this study,

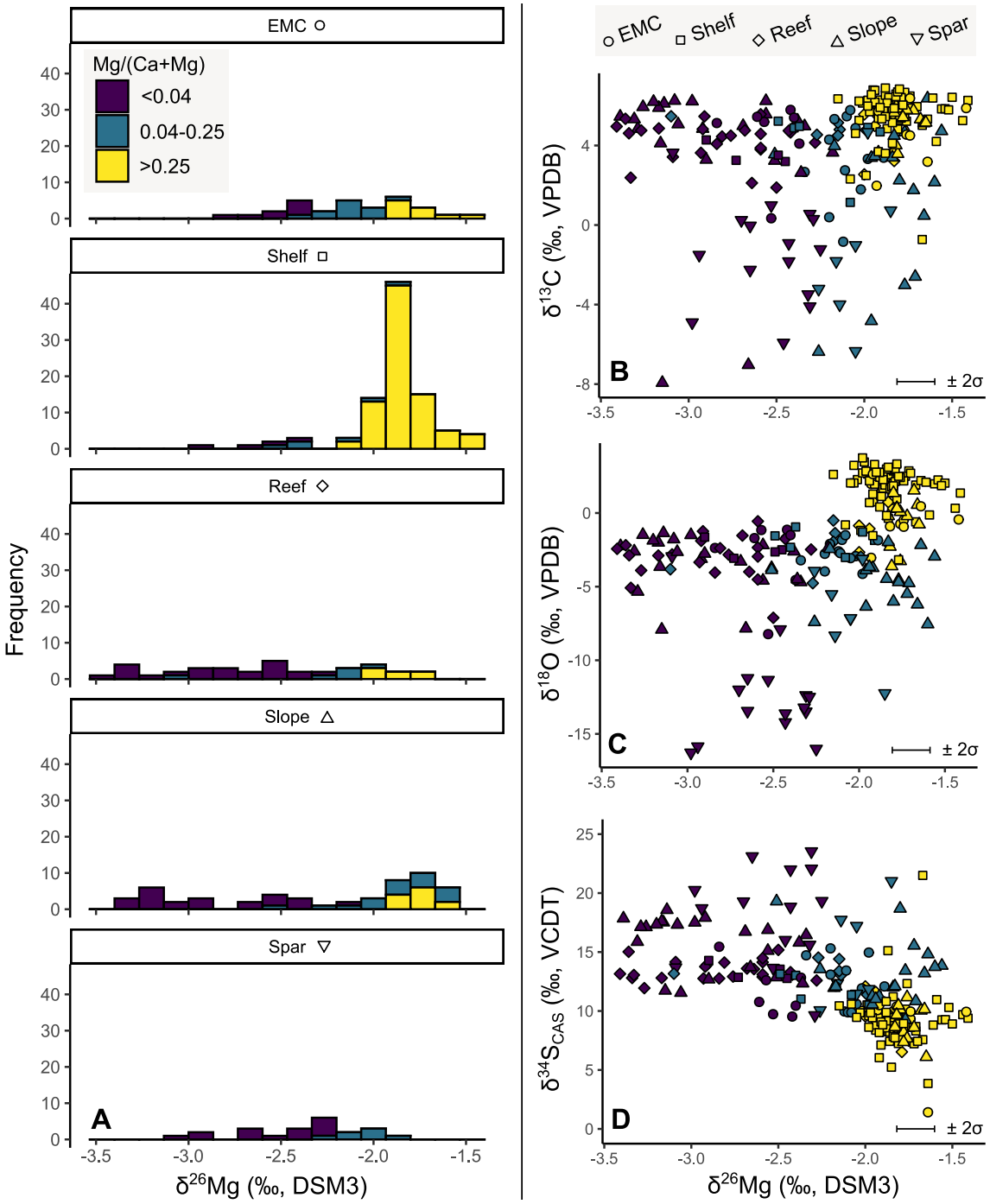

Fig. 5. Comparison of $\delta^{26}Mg$ (this study) with existing data (Present et al., 2019). (A) $\delta^{26}Mg$ histograms by facies group; (B-D) $\delta^{26}Mg$ versus $\delta^{13}C$, $\delta^{18}O$, and $\delta^{34}S_{CAS}$. Symbols correspond to facies tracts and are color coded by Mg/(Ca + Mg).

$-2.75 \pm 0.34‰$, perhaps indicating that the majority of recrystallized calcites precipitated from a fluid that was minimally evolved from seawater, with respect to $\delta^{26}Mg$. However, the most ^{26}Mg-depleted calcites in the slope and reef likely inherited some of their Mg from primary calcite bioclasts (i.e., recrystallized in more sediment-buffered conditions), which in general have larger $\delta^{26}Mg$ fractionations from seawater (Mavromatis et al., 2013; Higgins and Schrag, 2015). Additionally, there is sedimentological evidence that some dolomitization of primary carbonates started before other primary carbonates recrystallized to low-Mg calcite in the reef and slope (Mutti and Simo, 1994; Melim and Scholle, 2002; Present et al., 2019), which could have made the samples that escaped dolomitization more likely to retain something closer to their precursor $\delta^{26}Mg$ upon their later recrystallization.

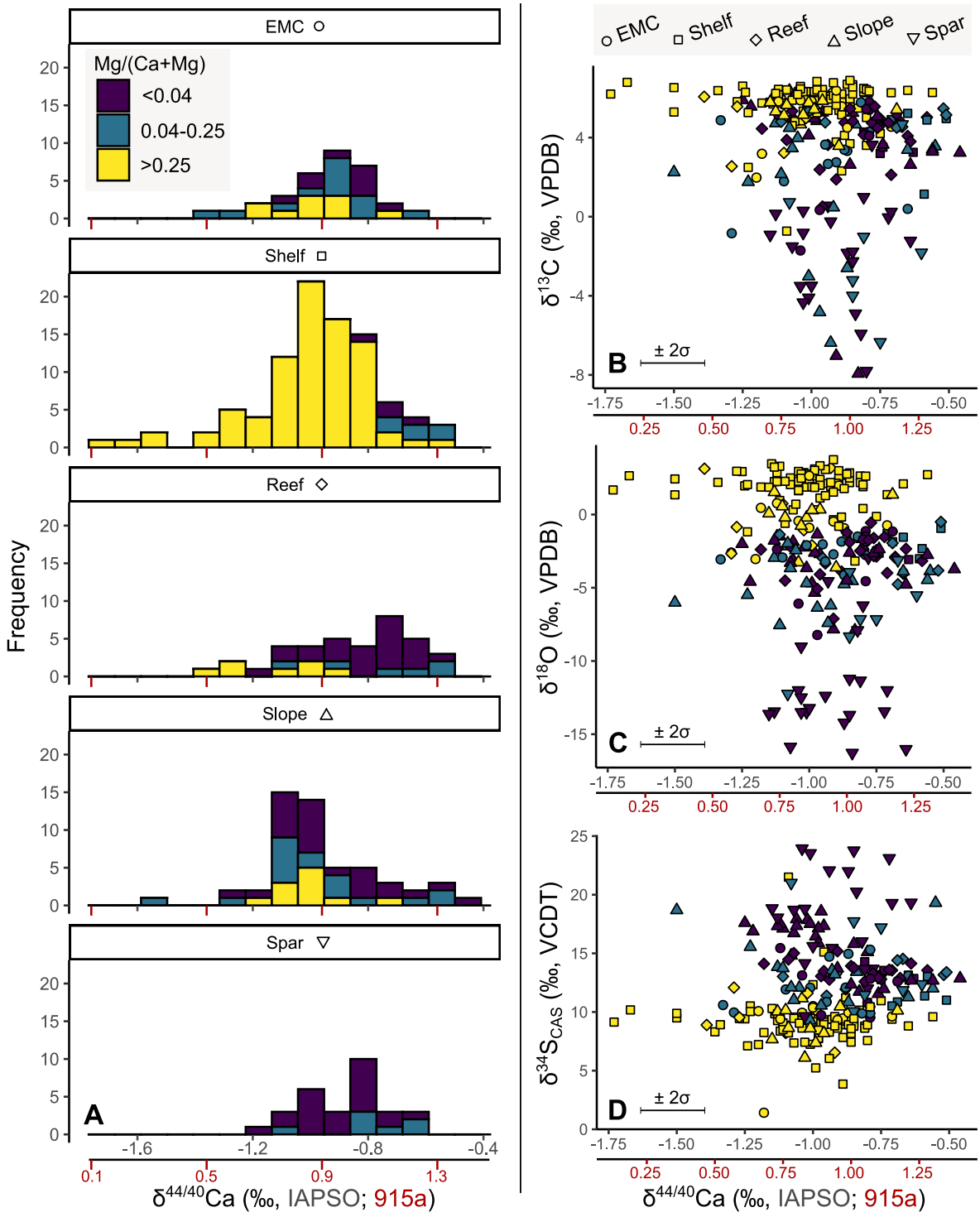

Fig. 6. Comparison of $\delta^{44/40}$Ca (this study) with existing data (Present et al., 2019). (A) $\delta^{44/40}$Ca histograms by facies group; (B-D) $\delta^{44/40}$Ca versus δ^{13}C, δ^{18}O, and $\delta^{34}S_{CAS}$. Symbols correspond to facies tracts and are color coded by Mg/(Ca + Mg).

Some δ^{26}Mg variability correlates with facies. For example, the dolomite-dominated samples of the slope facies tract are ~0.2‰ enriched in ^{26}Mg relative to the average dolomite-dominated sample from the shelf facies tract (Fig. 5A). This is likely to reflect more sediment-buffered conditions in the slope facies, which along with upstream precipitation of ^{26}Mg-depleted phases may have led to ^{26}Mg-enrichment of the dolomitizing fluid by Rayleigh distillation and slightly elevated δ^{26}Mg of dolomites along the fluid flow path.

The $\delta^{44/40}$Ca values paint a more complex picture of diagenesis in the Capitan Reef. Firstly, both calcite- and

dolomite-dominated samples display a broad range of $\delta^{44/40}$Ca values (Fig. 3), indicating that the mineralogical endmembers reflect a variety of different conditions or initial compositions. Additionally, dolomite-dominated samples can be variably depleted in ^{44}Ca relative to calcite-dominated samples in the same facies group – particularly on the shelf, where dolomitization was most pervasive (Fig. 6). This observation indicates a larger and more variable isotopic fractionation between seawater Ca^{2+} and dolomites than seawater Ca^{2+} and calcites. One possibility is that the primary sediment was a local source of Ca during dolomitization along the fluid flow path, through the substitution of Mg^{2+} for Ca^{2+}, in addition to the influx of seawater Ca^{2+}. However, the shelf dolomites and calcites were likely precipitated in an open-system environment where Ca transport was advection-dominated [i.e., by density-driven refluxing brines (Melim and Scholle, 2002)], and relatively fluid-buffered with respect to $\delta^{44/40}$Ca. As a result, it is possible that the variable calcite–dolomite $\delta^{44/40}$Ca offset reflects varying extents of dolomitization and/or variation in the fractionation factor during dolomitization, driven by variable precipitation rates or Ca^{2+}:CO_3^{2-} ratios in the pore-fluids (Tang et al., 2008; Mills et al., 2021). Variability in the Ca isotope fractionation factor during dolomitization is supported by the relatively invariant $\delta^{34}S_{CAS}$ and δ^{26}Mg values of the dolomites (Present et al., 2019), indicating that dolomites were fluid-buffered by seawater-derived brines.

Variability in $\delta^{44/40}$Ca values within the non-sparry calcite-dominated samples appears to correspond to variation in Sr/(Ca + Mg), δ^{13}C, and $\delta^{34}S_{CAS}$, which maps onto facies tracts (Fig. 7). Interpreting these observations with a diagenetic model, modified from Ahm et al. (2018), allows for the determination of and detailed comparison between fluid- versus rock-buffered diagenetic calcite endmembers – in addition to their percent recrystallization [based on Sr/(Ca + Mg)] – in a multi-proxy phase space. Here, we show that this approach provides an internally consistent, mechanistic, and semi-quantitative understanding of $\delta^{34}S_{CAS}$ behavior during early marine diagenesis along a shelf-basin transect. Additionally, the richness of the data allows us to disentangle the primary seawater signal (e.g., the concentration and isotopic composition of seawater SO_4^{2-}), allowing for a greater understanding of the ancient sulfur cycle. We used the results of a sensitivity analysis to determine suitable values for various input parameters (initial mineralogy, $[SO_4^{2-}]_{seawater}$, $[Ca^{2+}]_{seawater}$, MSR rate, the number of boxes ('n'), and the Ca isotopic fractionation factor for recrystallization; Fig. S2-7).

Fig. 7 shows crossplots of $\delta^{44/40}$Ca and $\delta^{34}S_{CAS}$ (Fig. 7A), and δ^{13}C and Sr/(Ca + Mg) (Fig. 7B), overlain by model-data fits of the compositions of fully recrystallized diagenetic calcite precipitated in a range of fluid- to sediment-buffered conditions. In both plots, different facies plot on a continuum between modeled fluid- and sediment-buffered diagenetic endmembers, close to the fully recrystallized limb, with very small contributions from the remaining primary precursor mineral. Specifically, samples from the slope facies tract plot closest to the more sediment-buffered endmember (box n), shelf samples plot closest to the fluid-buffered endmember (box 1), and reef samples plot in an intermediate position. The data indicate that Permian seawater had a $\delta^{44/40}$Ca value of greater than −0.4‰

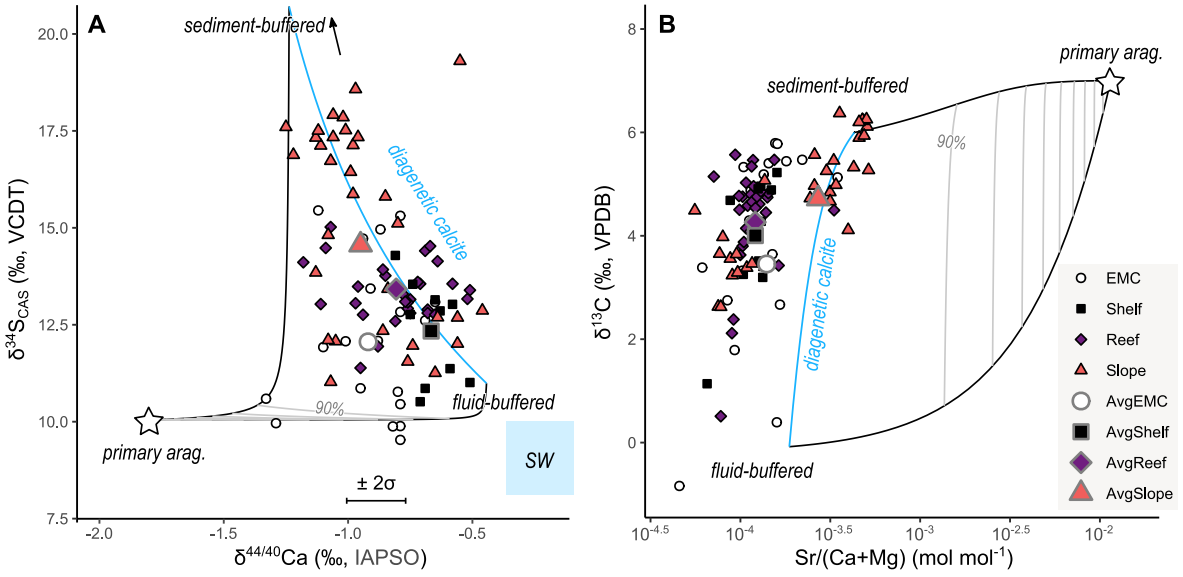

Fig. 7. Diagenetic model fits of, (A) $\delta^{44/40}$Ca and $\delta^{34}S_{CAS}$, and (B) δ^{13}C and Sr/(Ca + Mg), for non-sparry, calcite-dominated samples. The blue shaded region labeled 'SW' indicates the inferred composition of Delaware Basin seawater/brine; the white star indicates the expected composition of primary aragonite given empirical fractionation factors. Note that the displayed primary aragonite δ^{13}C composition is a maximum estimate – primary aragonite in shelf settings was likely several per mil enriched relative to reef and slope settings (Rivers et al., 2019; Present et al., 2019; Smith et al., 2020). The two black curves indicate the evolution of sediment- and fluid-buffered endmembers during progressive aragonite neomorphism; Gray curves are recrystallization deciles (10–90%) and the blue line indicates full recrystallization, i.e., diagenetic calcite. All these samples are ~100% recrystallized, so the spread in the data is not caused by varying degrees of recrystallization.

(IAPSO), likely closer to −0.2‰ (Fig. 7A). This is consistent with estimates of Permian seawater $\delta^{44/40}$Ca from evaporites (Blättler and Higgins, 2014).

EMCs plot slightly away from the main shelf–reef–slope trend in Fig. 7A (notably ^{44}Ca-depleted relative to seawater, but with the most seawater-like $\delta^{34}S_{CAS}$), albeit closest to the shelf samples. This indicates that although these cements were likely fluid-buffered with respect to δ^{34}S (as expected for crystals growing directly in contact with seawater), a parameter other than the degree of fluid-sediment buffering generated the $\delta^{44/40}$Ca variability. EMCs either, (1) were additionally subject to larger or more variable isotopic fractionations between primary mineral and fluid (Tang et al., 2008; Mills et al., 2021), (2) did not fully recrystallize (Chafetz et al., 2008), or (3) had a negative isotopic fractionation from the diagenetic fluid during recrystallization (Bradbury and Turchyn, 2018; Mills et al., 2021). Neither explanation 1 nor 2 is strongly supported by the Sr/(Ca + Mg) ratios of EMCs, which are very low, albeit slightly higher than those of reef and shelf samples (Fig. 7B). Therefore, explanation 3 [involving an inferred negative fractionation between pore water fluid and diagenetic mineral, −0.2 to −0.5‰ (Bradbury and Turchyn, 2018; Mills et al., 2021); Fig. 7A, S7] is the most plausible for the $\delta^{44/40}$Ca values of the EMCs.

4.2. Constraints on Permian seawater $[Ca^{2+}]$:$[SO_4^{2-}]$

The offset between the sulfur isotope ratio of CAS in recrystallized carbonates and that of seawater ($\Delta^{34}S_{CAS\text{-}seawater}$) is predominantly a function of the relative rates/timescales of carbonate recrystallization versus MSR below the sediment–water interface (Rennie and Turchyn, 2014). In modern sediments, the rates of both recrystallization and organoclastic MSR have been observed to decay exponentially with increasing burial depth (Middleburg, 1989; Fantle and DePaolo, 2007). The rates of sulfate reduction [mostly a function of the initial concentration of labile organic matter; (Boudreau and Westrich, 1984)] and transport of new sulfate into pore waters control the timescale of sulfate drawdown in the pore fluid. The timescale of carbonate recrystallization is typically on the order of millions of years for typical deep-sea sediments (Fantle et al., 2010), and approaching 1 Myr for more rapidly accumulating platform sediments (Higgins et al., 2018; Staudigel et al., 2021). Evidence from the geologic record suggests much shorter timeframes (sub-100 Kyr) timeframes for early diagenetic dolomitization and lithification (Manche and Kaczmarek, 2019; Ning et al., 2020), and stratal geometries of dolomite in the Capitan Reef Complex indicate that dolomitization occurred on the timescale of high frequency sequences (sub-Myr) (Mutti and Simo, 1993; Mutti and Simo, 1994; Garcia-Fresca et al., 2012; Wu et al., 2020). An ideal ratio exists between the rates of MSR and recrystallization that will result in maximally elevated $\delta^{34}S_{CAS}$ values, with a maximal $\Delta^{34}S_{CAS\text{-}seawater}$ of between 1 and 3‰ for three modern sites in slope settings (Rennie and Turchyn, 2014). Ratios that are either too high or too low would result in very little incorporation of ^{34}S-enriched sulfate into diagenetic calcite because pore water sulfate would either be consumed prior to substantive recrystallization (recrystallization/MSR ratio too low) or would not diverge from the isotopic composition of seawater sulfate prior to complete recrystallization (recrystallization/MSR ratio too high). In addition to recrystallization and MSR, the magnitude of $\Delta^{34}S_{CAS\text{-}seawater}$ in geologic carbonates also depends on other factors that influence the drawdown of sulfate in pore waters, including $[SO_4^{2-}]_{seawater}$ and the depth of the redox-cline, as a function of bottom water $[O_2]$.

Given that the Capitan Reef Complex samples span a shelf-basin transect, we expected them to capture a large range (from fully fluid- to more sediment-buffered) of $\delta^{34}S_{CAS}$ and $\delta^{44/40}$Ca values. If seawater $\delta^{34}S_{sulfate}$ was + 9‰ (Present et al., 2019), $\Delta^{34}S_{CAS\text{-}seawater}$ ranges from 1 to 10‰ for the calcite-dominated samples (excluding sparry cements) (Fig. 7A). The smallest $\Delta^{34}S_{CAS\text{-}seawater}$ values occur in EMCs on the shelf and the largest occur in the slope facies tract (particularly the toe-of-slope). This sample set therefore provides a new opportunity to set constraints on the major ion seawater chemistry of the Delaware Basin. We use a numerical model to explore the key parameters that determine the geochemical spread of data in the $\delta^{34}S_{CAS}$/$\delta^{44/40}$Ca phase space. To explain the observed ^{34}S-enrichment (Fig. 7A), MSR and recrystallization must overlap in time and space (Rennie and Turchyn, 2014). The model predicts that the relative rates of MSR and recrystallization control the spread of $\delta^{34}S_{CAS}$ values (but not $\delta^{44/40}$Ca values; Fig. S5) as a higher rate of MSR results in greater ^{34}S-enrichment of residual sulfate along the fluid flow path. Alternatively, lowering seawater (and pore water) $[SO_4^{2-}]$ could produce a similar pattern because of the effect of reservoir size on Rayleigh distillation (Fig. S2). Despite being highly productive environments, carbonate platforms typically preserve low organic matter concentrations (Geyman and Maloof, 2019), mostly due to high rates of aerobic respiration near the sediment–water interface (Bowles et al., 2014). Similarly, these rocks have very little preserved organic matter [e.g., the Capitan Fm. contains on average < 0.5 wt.% organic matter; (Mazzullo and Cys, 1983)]. Thus, it is hard to imagine the Capitan Reef having supported high net rates of sulfate reduction throughout the sediment column, and it seems likely that low seawater $[SO_4^{2-}]$ contributed to the spread of the $\delta^{34}S_{CAS}$ data. Holding all other model input parameters (rates, concentrations and isotopic compositions) constant and at reasonable values based on literature estimates (see Table 1), we varied $[SO_4^{2-}]$ between 13 and 52 mM such that the $[Ca^{2+}]$:$[SO_4^{2-}]$ ratio varied between 1.0 [upper constraint from evaporite fluid inclusions (Horita et al., 2002)] and 0.25. We find that a $[Ca^{2+}]$:$[SO_4^{2-}]$ ratio approaching 1 (likely close to 0.8) gives the best model-data fit (Fig. 8) as the modeled fully recrystallized diagenetic calcite spans the range of both the $\delta^{44/40}$Ca and $\delta^{34}S_{CAS}$ data with an appropriate slope. Our $[Ca^{2+}]$:$[SO_4^{2-}]$ ratio estimate is at the upper end of estimates from fluid inclusions (Horita

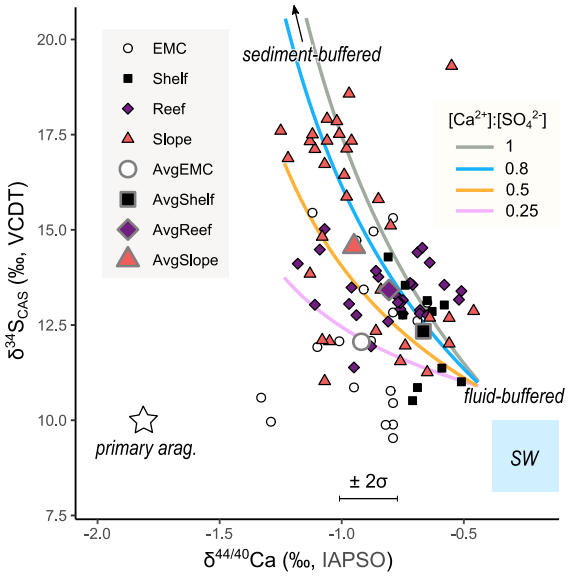

Fig. 8. Illustration of how lowering $[Ca^{2+}]$:$[SO_4^{2-}]_{seawater}$ (by raising $[SO_4^{2-}]_{seawater}$) affects predictions for the $\delta^{34}S_{CAS}$ and $\delta^{44/40}Ca$ values by decreasing the slope of recrystallized/diagenetic calcite. For these conditions, a $[Ca^{2+}]$:$[SO_4^{2-}]_{seawater}$ between 0.5 and 1 (i.e., 13 mM < $[SO_4^{2-}]_{seawater}$ < 26 mM) is most consistent with the data – this is because a high $[SO_4^{2-}]_{seawater}$ results in slower drawdown and isotopic distillation of pore water $[SO_4^{2-}]$ relative to the rate of recrystallization, minimizing the degree of ^{34}S-enrichment of diagenetic CAS relative to seawater-SO_4^{2-}. If a smaller MSR rate constant than that assumed here [3e-3 y^{-1} (Canfield, 1991)] were used, the corresponding slopes of the model outputs would be shallower, and vice versa (see Fig. S5). If a more positive Ca fractionation factor of recrystallization than that assumed here [−0.2‰ (Mills et al., 2021)] were used, the model outputs would be shifted to more positive $\delta^{44/40}Ca$ values, with slightly shallower slopes, and vice versa (see Fig. S7).

et al., 2002), and roughly two to three times that observed in the modern ocean – however it is not so high as to be inconsistent with the presence of sulfate evaporites and sulfate-rich fluid inclusions in the Delaware Basin (Leslie et al., 1997; Horita et al., 2002).

4.3. Implications for the origins of the early marine cements of the Capitan Reef Complex

Our interpreted $[Ca^{2+}]$:$[SO_4^{2-}]$ value for Permian seawater could help explain the anomalous presence of abundant early marine (botryoidal and isopachous) cements in the Capitan Reef Complex – a style of cementation famously compared to Precambrian examples by Grotzinger and Knoll (1995). Those authors suggested that upwelling anoxic deep waters could have provided a source of alkalinity for seafloor carbonate precipitation. Due to the biological pump, upwelling waters would be expected to have more ^{13}C-depleted dissolved inorganic carbon (DIC) than surface waters – however, we see no evidence of contribution of a ^{13}C-depleted DIC pool to any subset of the carbonates deposited during this time interval (excluding those impacted by burial diagenesis). Instead, we infer that primary carbonates must have had a $\delta^{13}C$ value of ~+5 – 7‰ [and possibly several per mil higher than this in evaporitic, supratidal shelf environments due to the greater degree of restriction (Rivers et al., 2019)], consistent with interpretations from previous studies (Given and Lohmann, 1985; Mutti and Simo, 1994; Smith et al., 2020) (Fig. 7B). The inferred enriched $\delta^{13}C$ value of platform aragonite is consistent with carbonate precipitation from a DIC pool that was ^{13}C-enriched due to either photosynthesis (Geyman and Maloof, 2019; Present et al., 2019) and/or CO_2 degassing caused by a combination of evaporation and carbonate precipitation in a restricted setting (Stiller et al., 1985; Beeler et al., 2020). To explain the differences in $\delta^{13}C$ between sediment- and fluid- buffered endmembers (Fig. 7B), DIC in pore waters must have been substantially ^{13}C-depleted relative to the water column [as expected from organic matter remineralization; (Meister et al., 2019)].

Based on the $\delta^{44/40}Ca$, $\delta^{34}S_{CAS}$ and $\delta^{13}C$ data for the Capitan Reef samples, rather than invoking an alkalinity influx for the extensive cement precipitation, we posit that an elevated $[Ca^{2+}]$:$[SO_4^{2-}]$ similar to that of the late Proterozoic contributed to the favorability of carbonate cement precipitation. As sulfate inhibits the precipitation of calcite and aragonite (Reddy and Nancollas, 1976; Sjoberg, 1978; Busenberg and Niel Plummer, 1985; Walter, 1986; Burton and Walter, 1987; Mucci et al., 1989), a lower $[SO_4^{2-}]_{seawater}$ in the Delaware Basin would have increased the kinetic favorability of early marine carbonate cement precipitation. In addition, a combination of the restrictedness of the depositional setting (Garber et al., 1989) and low sea level (Ridgwell, 2005; Smith et al., 2021) may have further increased the basin wide saturation state of aragonite. Higher temperatures in the shallow waters overlying the shelf and reef facies would have particularly favored the precipitation of aragonite over calcite (Burton and Walter, 1987). However, on the shelf, higher rates of aerobic respiration might have lowered the aragonite saturation state below the sediment–water interface (Bergmann et al., 2013), opposing the preservation of aragonite and favoring early diagenetic dolomitization (Rivers et al., 2021).

5. CONCLUSIONS

The $\delta^{34}S_{CAS}$ values of the Permian Capitan Reef carbonates are highly sensitive to the degree of fluid- vs. sediment-buffering of the environment of carbonate precipitation, which can be assessed using other carbonate-based geochemical proxies such as $\delta^{44/40}Ca$, $\delta^{26}Mg$ and Sr/(Ca + Mg). Because sulfur isotopes are sensitive to microbial sulfur cycling processes such as MSR, whereas other proxies are mostly subject to recrystallization of primary carbonate minerals, we can constrain the spatial and/or temporal overlap in the processes of MSR and carbonate recrystallization from the correlations between the proxies. Most notably, for non-sparry calcites, $\delta^{44/40}Ca$ and $\delta^{34}S_{CAS}$ are negatively correlated, a relationship that maps onto facies context. In contrast, dolomites consistently record seawater $\delta^{34}S_{sulfate}$, despite having variable $\delta^{44/40}Ca$ values (likely due to variable precipitation rates or Ca^{2+}:CO_3^{2-} ratios). The relative lack of $\delta^{26}Mg$ variability

in the dolomites emphasizes that dolomitization occurred during early, fluid-buffered diagenesis, locking in the signal of seawater/brine $\delta^{34}S_{sulfate}$. Our results demonstrate that $\delta^{44/40}Ca$ and $\delta^{26}Mg$ can be powerful tools for identifying fluid-buffered rocks, which – so long as the fluid is syndepositional seawater – may record seawater $\delta^{34}S_{sulfate}$, even in the absence of facies context. Furthermore, we show that the richness of the data in the Ca-S isotopic phase space enables semi-quantitative assessment of water column $[Ca^{2+}]$:$[SO_4^{2-}]$ ratios. For the Capitan Reef, an estimated $[Ca^{2+}]$:$[SO_4^{2-}]$ ratio of ~1 is the most parsimonious explanation for the presence of ubiquitous pre-Cambrian-like early marine cements. Finally, looking to the broader rock record prior to the availability of pelagic drill core sediments, we can use a paired $\delta^{44/40}Ca$ – $\delta^{26}Mg$ approach to identify early diagenetic dolomites and the most fluid-buffered calcites, both of which are likelier than sediment-buffered calcites to record seawater $\delta^{34}S_{sulfate}$ in their $\delta^{34}S_{CAS}$ values.

Declaration of Competing Interest

The authors declare that they have no known competing financial interests or personal relationships that could have appeared to influence the work reported in this paper.

ACKNOWLEDGEMENTS

The authors thank two anonymous reviewers and the associate editor, Adrian Immenhauser, for their constructive and insightful comments, which greatly improved this manuscript. We thank the members of the Blättler group at the University of Chicago for their support and discussions during this project, particularly in the break enforced by the Covid-19 crisis. This work was supported by a grant from the Simons Foundation to ASCA (SCOL 611878). Samples from Guadalupe Mountains National Park were collected with permits GUMO-2012-SCI-0014, GUMO-2013-SCI-0016, and GUMO-2016-SCI-0010.

RESEARCH DATA

All data presented in this study can be found in the attached file named Research Data. The model code is available from the authors upon request.

APPENDIX A. SUPPLEMENTARY MATERIAL

Supplementary data to this article can be found online at https://doi.org/10.1016/j.gca.2022.04.027.

REFERENCES

Adams J. E. and Rhodes M. L. (1960) Dolomitization by seepage refluxion. *Am. Assoc. Pet. Geol. Bull.* **44**, 1912–1920.

Ahm A. S. C., Bjerrum C. J., Blättler C. L., Swart P. K. and Higgins J. A. (2018) Quantifying early marine diagenesis in shallow-water carbonate sediments. *Geochim. Cosmochim. Acta* **236**, 140–159.

Ahm A. S. C., Maloof A. C., Macdonald F. A., Hoffman P. F., Bjerrum C. J., Bold U., Rose C. V., Strauss J. V. and Higgins J. A. (2019) An early diagenetic deglacial origin for basal Ediacaran "cap dolostones". *Earth Planet. Sci. Lett.* **506**, 292–307.

Algeo T. J., Luo G. M., Song H. Y., Lyons T. W. and Canfield D. E. (2015) Reconstruction of secular variation in seawater sulfate concentrations. *Biogeosciences* **12**, 2131–2151.

Assereto R. L. and Kendall C. G. (1977) Nature, origin and classification of peritidal tepee structures and related breccias. *Sedimentology* **24**, 153–210.

Barkan Y., Paris G., Webb S. M., Adkins J. F. and Halevy I. (2020) Sulfur isotope fractionation between aqueous and carbonate-associated sulfate in abiotic calcite and aragonite. *Geochim. Cosmochim. Acta* **280**, 317–339.

Beeler S. R., Gomez F. J. and Bradley A. S. (2020) Controls of extreme isotopic enrichment in modern microbialites and associated abiogenic carbonates. *Geochim. Cosmochim. Acta* **269**, 136–149.

Bergmann K. D., Grotzinger J. P. and Fischer W. W. (2013) Biological influences on seafloor carbonate precipitation. *Palaios* **28**, 99–115.

Berner R. A. (1989) Biogeochemical cycles of carbon and sulfur and their effect on atmospheric oxygen over phanerozoic time. *Glob. Planet. Change* **1**, 97–122.

Bialik O. M., Wang X., Zhao S., Waldmann N. D., Frank R. and Li W. (2018) Mg isotope response to dolomitization in hinterland-attached carbonate platforms: Outlook of $\delta^{26}Mg$ as a tracer of basin restriction and seawater Mg/Ca ratio. *Geochim. Cosmochim. Acta* **235**, 189–207.

Bishop J. W., Osleger D. A., Montãez I. P. and Sumner D. Y. (2014) Meteoric diagenesis and fluid-rock interaction in the middle Permian capitan backreef: Yates formation, slaughter canyon, New Mexico. *Am. Assoc. Pet. Geol. Bull.* **98**, 1495–1519.

Blättler C. L., Claire M. W., Prave A. R., Kirsimäe K., Higgins J. A., Medvedev P. V., Romashkin A. E., Rychanchik D. V., Zerkle A. L., Paiste K., Kreitsmann T., Millar I. L., Hayles J. A., Bao H., Turchyn A. V., Warke M. R. and Lepland A. (2018) Two-billion-year-old evaporites capture Earth's great oxidation. *Science (80-.)* **360**, 320–323.

Blättler C. L. and Higgins J. A. (2014) Calcium isotopes in evaporites record variations in Phanerozoic seawater SO_4 and Ca. *Geology* **42**, 711–714.

Blättler C. L., Miller N. R. and Higgins J. A. (2015) Mg and Ca isotope signatures of authigenic dolomite in siliceous deep-sea sediments. *Earth Planet. Sci. Lett.* **419**, 32–42.

Borer J. M. and Harris P. M. (1991) Lithofacies and cyclicity of the Yates Formation, Permian Basin: Implications for reservoir heterogeneity. *Am. Assoc. Pet. Geol. Bull.* **75**, 726–779.

Boudreau B. P. and Westrich J. T. (1984) The dependence of bacterial sulfate reduction on sulfate concentration in marine sediments. *Geochim. Cosmochim. Acta* **48**, 2503–2516.

Bowles M. W., Mogolĺon J. M., Kasten S., Zabel M. and Hinrichs K. U. (2014) Global rates of marine sulfate reduction and implications for sub-sea-floor metabolic activities. *Science (80-.)* **344**, 889–891.

Bradbury H. J. and Turchyn A. V. (2018) Calcium isotope fractionation in sedimentary pore fluids from ODP Leg 175: Resolving carbonate recrystallization. *Geochim. Cosmochim. Acta* **236**, 121–139.

Budd D. A., Frost E. L., Huntington K. W. and Allwardt P. F. (2013) Syndepositional deformation features in high-relief carbonate platforms: Long-lived conduits for diagenetic fluids. *J. Sediment. Res.* **83**, 12–36.

Burdett J. W., Arthur M. A. and Richardson M. (1989) A Neogene seawater sulfur isotope age curve from calcareous pelagic microfossils. *Earth Planet. Sci. Lett.* **94**, 189–198.

Burton E. A. and Walter L. M. (1987) Relative precipitation rates of aragonite and Mg calcite from seawater: temperature or carbonate ion control? *Geology* **15**, 111–114.

Busenberg E. and Niel Plummer L. (1985) Kinetic and thermodynamic factors controlling the distribution of SO_3^{2-} and Na+ in calcites and selected aragonites. *Geochim. Cosmochim. Acta* **49**, 713–725.

Canfield D. E. (2001) Biogeochemistry of sulfur isotopes. *Rev. Mineral. Geochem.* **43**, 607–636.

Canfield D. E. (1991) Sulfate reduction in deep-sea sediments. *Am. J. Sci.* **291**, 177–188.

Canfield D. E. and Farquhar J. (2009) Animal evolution, bioturbation, and the sulfate concentration of the oceans. *Proc. Natl. Acad. Sci.* **106**, 8123–8127.

Canfield D. E. and Teske A. (1996) Late proterozoic rise in atmospheric oxygen concentration inferred from phylogenetic and sulphur-isotope studies. *Nature* **382**, 127–132.

Chafetz H. S., Wu Z., Lapen T. J. and Milliken K. L. (2008) Geochemistry of preserved Permian aragonitic cements in the tepees of the Guadalupe Mountains, West Texas and New Mexico, U.S.A. *J. Sediment. Res.* **78**, 187–198.

Claypool G. E., Holser W. T., Kaplan I. R., Sakai H. and Zak I. (1980) The age curves of sulfur and oxygen isotopes in marine sulfate and their mutual interpretation. *Chem. Geol.* **28**, 199–260.

Coplen T. B. (2011) Guidelines and recommended terms for expression of stable-isotope-ratio and gas-ratio measurement results. *Rapid Commun. Mass Spectrom.* **25**, 2538–2560.

Crockford P. W., Kunzmann M., Blättler C. L., Kalderon-Asael B., Murphy J. G., Ahm A. S., Sharoni S., Halverson G. P., Planavsky N. J., Halevy I. and Higgins J. A. (2021) Reconstructing Neoproterozoic seawater chemistry from early diagenetic dolomite. *Geology* **49**, 442–446.

Cys J. M., Toomey D. F., Brezina J. L., Greenwood E., Groves D. B., Klement K. W., Kullman J. D., McMillan T. L., Schmidt V., Sneed E. D. and Wagner L. H. (1977) Capitan reef - Evolution of a concept. In *Upper Guadalupian Facies, Permian Reef Complex, Guadalupe Mountains, New Mexico and west Texas, 1977 field conference guidebook* (eds. M. E. Hileman and S. J. Mazzullo). Permian Basin Section SEPM Publication. Permian Basin Section SEPM, Midland, Texas, pp. 201–322.

Ding T., Bai R., Li Y., Wan D., Zou X. and Zhang Q. (1999) Determination of the absolute $^{32}S/^{34}S$ ratio of IAEA-S-1 reference material and V-CDT sulfur isotope standard. *Sci. China Ser. D Earth Sci.* **42**, 45–51.

Eldridge D. L., Guo W. and Farquhar J. (2016) Theoretical estimates of equilibrium sulfur isotope effects in aqueous sulfur systems: Highlighting the role of isomers in the sulfite and sulfoxylate systems. *Geochim. Cosmochim. Acta* **195**, 171–200.

Esteban M. and Pray L. (1983) Pisoids and pisolite facies (Permian), Guadalupe Mountains, New Mexico and West Texas. In *Coated grains* (ed. T. M. Peryt). Springer-Verlag, Berlin, Germany, pp. 503–537.

Esteban M. and Pray L. C. (1977) Origin of the pisolite facies of the shelf crest. In *Upper Guadalupian Facies, Permian Reef Complex, Guadalupe Mountains, New Mexico and west Texas, 1977 Field Conference Guidebook* (eds. M. E. Hileman and S. J. Mazzullo). Permian Basin Section SEPM Publication. Permian Basin Section SEPM, Midland, Texas, pp. 479–484.

Fantle M. S. and DePaolo D. J. (2007) Ca isotopes in carbonate sediment and pore fluid from ODP Site 807A: The Ca^{2+}(aq)-calcite equilibrium fractionation factor and calcite recrystallization rates in Pleistocene sediments. *Geochim. Cosmochim. Acta* **71**, 2524–2546.

Fantle M. S., Maher K. M. and Depaolo D. J. (2010) Isotopic approaches for quantifying the rates of marine burial diagenesis. *Rev. Geophys.* **48**, RG3002.

Farkaš J., Böhm F., Wallmann K., Blenkinsop J., Eisenhauer A., van Geldern R., Munnecke A., Voigt S. and Veizer J. (2007) Calcium isotope record of Phanerozoic oceans: Implications for chemical evolution of seawater and its causative mechanisms. *Geochim. Cosmochim. Acta* **71**, 5117–5134.

Fichtner V., Strauss H., Immenhauser A., Buhl D., Neuser R. D. and Niedermayr A. (2017) Diagenesis of carbonate associated sulfate. *Chem. Geol.* **463**, 61–75.

Fike D. A., Bradley A. S. and Rose C. V. (2015) Rethinking the ancient sulfur cycle. *Annu. Rev. Earth Planet. Sci.* **43**, 593–622.

Fike D. A., Grotzinger J. P., Pratt L. M. and Summons R. E. (2006) Oxidation of the Ediacaran ocean. *Nature* **444**, 744–747.

Frost E. L., Budd D. A. and Kerans C. (2013) Syndepositional deformation in a high-relief carbonate platform and its effect on early fluid flow as revealed by dolomite patterns. *J. Sediment. Res.* **82**, 913–932.

Galy A., Yoffe O., Janney P. E., Williams R. W., Cloquet C., Alard O., Halicz L., Wadhwa M., Hutcheon I. D., Ramon E. and Carignan J. (2003) Magnesium isotope heterogeneity of the isotopic standard SRM980 and new reference materials for magnesium-isotope-ratio measurements. *J. Anal. At. Spectrom.* **18**, 1352–1356.

Garber R. A., Grover G. A. and Harris P. M. (1989) Geology of the Capitan Shelf Margin - Subsurface Data from the Northern Delaware Basin. In *Subsurface and Outcrop Examination of the Capitan Shelf Margin, Northern Delaware Basin*. SEPM (Society for Sedimentary Geology), pp. 3–271.

Garcia-Fresca B., Jerry L. F., Sharp J. M. and Kerans C. (2012) Outcrop-constrained hydrogeological simulations of brine reflux and early dolomitization of the Permian San Andres Formation. *Am. Assoc. Pet. Geol. Bull.* **96**, 1757–1781.

Garrels R. M. and Lerman A. (1981) Phanerozoic cycles of sedimentary carbon and sulfur. *Proc. Natl. Acad. Sci. U. S. A.* **78**, 4652–4656.

Geyman E. C. and Maloof A. C. (2019) A diurnal carbon engine explains ^{13}C-enriched carbonates without increasing the global production of oxygen. *Proc. Natl. Acad. Sci. U. S. A.* **116**, 24433–24439.

Given R. K. and Lohmann K. C. (1985) Derivation of the original isotopic composition of Permian marine cements. *J. Sediment. Res.* **55**, 430–439.

Given R. K. and Lohmann K. C. (1986) Isotopic evidence for the early meteoric diagenesis of the reef facies, Permian Reef Complex of west Texas and New Mexico. *J. Sediment. Petrol.* **56**, 183–193.

Grotzinger J. P. and Knoll A. H. (1995) Anomalous carbonate precipitates: is the Precambrian the key to the Permian? *Palaios* **10**, 578–596.

Gussone N., Böhm F., Eisenhauer A., Dietzel M., Heuser A., Teichert B. M. A., Reitner J., Wörheide G. and Dullo W. C. (2005) Calcium isotope fractionation in calcite and aragonite. *Geochim. Cosmochim. Acta* **69**, 4485–4494.

Henderson G. M., Slowey N. C. and Haddad G. A. (1999) Fluid flow through carbonate platforms: constraints from $^{234}U/^{238}U$ and Cl^- in Bahamas pore-waters. *Earth Planet. Sci. Lett.* **169**, 99–111.

Higgins J. A., Blättler C. L., Lundstrom E. A., Santiago-Ramos D. P., Akhtar A. A., Crüger Ahm A. S., Bialik O., Holmden C., Bradbury H., Murray S. T. and Swart P. K. (2018) Mineralogy, early marine diagenesis, and the chemistry of shallow-water carbonate sediments. *Geochim. Cosmochim. Acta* **220**, 512–534.

Higgins J. A. and Schrag D. P. (2015) The Mg isotopic composition of Cenozoic seawater - evidence for a link between Mg-clays, seawater Mg/Ca, and climate. *Earth Planet. Sci. Lett.* **416**, 73–81.

Hill C. A. (1990) Sulfuric acid speleogenesis of Carlsbad Cavern and its relationship to hydrocarbons, Delaware Basin, New Mexico and Texas. *Am. Assoc. Pet. Geol. Bull.* **74**, 1685–1694.

Hippler D., Schmitt A. D., Gussone N., Heuser A., Stille P., Eisenhauer A. and Nägler T. F. (2003) Calcium isotopic composition of various reference materials and seawater. *Geostand. Newsl.* **27**, 13–19.

Holser W. T. and Kaplan I. R. (1966) Isotope geochemistry of sedimentary sulfates. *Chem. Geol.* **1**, 93–135.

Horita J., Zimmermann H. and Holland H. D. (2002) Chemical evolution of seawater during the Phanerozoic: Implications from the record of marine evaporites. *Geochim. Cosmochim. Acta* **66**, 3733–3756.

Jochum K. P., Nohl U., Herwig K., Lammel E., Stoll B. and Hofmann A. W. (2005) GeoReM: A new geochemical database for reference materials and isotopic standards. *Geostand. Geoanal. Res.* **29**, 333–338.

Jones D. S., Brothers R. W., Ahm A. S. C., Slater N., Higgins J. A. and Fike D. A. (2020) Sea level, carbonate mineralogy, and early diagenesis controlled $\delta^{13}C$ records in Upper Ordovician carbonates. *Geology* **48**, 194–199.

Kah L. C., Lyons T. W. and Frank T. D. (2004) Low marine sulphate and protracted oxygenation of the Proterozoic biosphere. *Nature* **431**, 834–838.

Kampschulte A. and Strauss H. (2004) The sulfur isotopic evolution of Phanerozoic seawater based on the analysis of structurally substituted sulfate in carbonates. *Chem. Geol.* **204**, 255–286.

Kendall C. G. S. C. (1969) An environmental Re-interpretation of the Permian Evaporite/Carbonate Shelf Sediments of the Guadalupe Mountains. *GSA Bull.* **80**, 2503–2526.

Kerans C. and Tinker S. W. (1999) Extrinsic stratigraphic controls on development of the capitan reef complex. In *Geologic Framework of the Capitan Reef*. SEPM (Society for Sedimentary Geology), pp. 15–36.

Kirkland D. W., Denison R. E. and Dean W. E. (2000) Parent Brine of the Castile Evaporites (Upper Permian), Texas and New Mexico. *J. Sediment. Res.* **70**, 749–761.

Koša E. and Hunt D. W. (2006) Heterogeneity in Fill and Properties of Karst-Modified Syndepositional Faults and Fractures: Upper Permian Capitan Platform, New Mexico, U. S.A. *J. Sediment. Res.* **76**, 131–151.

Lambert L. L. (2002) Latest Guadalupian (Middle Permian) conodonts and foraminifers from West Texas. *Micropaleontology* **48**, 343–364.

Leavitt W. D., Halevy I., Bradley A. S. and Johnston D. T. (2013) Influence of sulfate reduction rates on the Phanerozoic sulfur isotope record. *Proc. Natl. Acad. Sci.* **110**, 11244–11249.

Leslie A. B., Harwood G. M. and Kendall A. C. (1997) Geochemical variations within a laminated evaporite deposit: Evidence for brine composition during formation of the Permian Castile Formation, Texas and New Mexico, USA. *Sediment. Geol.* **110**, 223–235.

Li W., Beard B. L., Li C., Xu H. and Johnson C. M. (2015) Experimental calibration of Mg isotope fractionation between dolomite and aqueous solution and its geological implications. *Geochim. Cosmochim. Acta* **157**, 164–181.

Li W., Chakraborty S., Beard B. L., Romanek C. S. and Johnson C. M. (2012) Magnesium isotope fractionation during precipitation of inorganic calcite under laboratory conditions. *Earth Planet. Sci. Lett.* **333–334**, 304–316.

Loyd S. J., Dickson J. A. D., Scholle P. A. and Tripati A. K. (2013) Extensive, uplift-related and non-fault-controlled spar precipitation in the Permian Capitan Formation. *Sediment. Geol.* **298**, 17–27.

Manche C. J. and Kaczmarek S. E. (2019) Evaluating reflux dolomitization using a novel high-resolution record of dolomite stoichiometry: A case study from the Cretaceous of central Texas, USA. *Geology* **47**, 586–590.

Mavromatis V., Gautier Q., Bosc O. and Schott J. (2013) Kinetics of Mg partition and Mg stable isotope fractionation during its incorporation in calcite. *Geochim. Cosmochim. Acta* **114**, 188–203.

Mazzullo S. J. (1980) Calcite pseudospar replacive of marine acicular aragonite, and implications for aragonite cement diagenesis. *J. Sediment. Res.* **50**, 409–422.

Mazzullo S. J. (1999) Paleoenvironments, Cyclicity, and Diagenesis in the Outer Shelf Tansill Formation in the Carlsbad Embayment (Dark Canyon), Northern Guadalupe Mountains, New Mexico. In *Geologic Framework of the Capitan Reef.* (eds. A. H. Saller, P. M. Harris, B. L. Kirkland and S. J. Mazzullo). SEPM Special Publication, pp. 107–128.

Mazzullo S. J. and Cys J. M. (1977) Submarine cements in Permian boundstones and reef-associated rocks, Guadalupe Mountains, west Texas and southeastern New Mexico. In *Upper Guadalupian Facies, Permian Reef Complex, Guadalupe Mountains, New Mexico and West Texas, 1977 Field Conference Guidebook* (eds. M. E. Hileman and S. J. Mazzullo). SEPM (Society for Sedimentary Geology), Midland, Texas, pp. 151–200.

Mazzullo S. J. and Cys J. M. (1983) Unusual Algal-Crystalline Carbonate Coated Grains from the Capitan Reef (Permian, Guadalupian), New Mexico, USA. In *Coated Grains*. Springer, Berlin Heidelberg, pp. 599–608.

Meister P., Liu B., Khalili A., Böttcher M. E. and Jørgensen B. B. (2019) Factors controlling the carbon isotope composition of dissolved inorganic carbon and methane in marine porewater: An evaluation by reaction-transport modelling. *J. Mar. Syst.* **200**, 103227.

Melim L. A. and Scholle P. A. (1989) Dolomitization Model for the Forereef Facies of the Permian Capitan Formation, Guadalupe Mountains, Texas-New Mexico. In *Subsurface and Outcrop Examination of the Capitan Shelf Margin, Northern Delaware Basin* (eds. P. M. Harris and G. A. Grover). SEPM Core Workshop. SEPM, San Antonio, Texas, pp. 407–413.

Melim L. A. and Scholle P. A. (2002) Dolomitization of the Capitan Formation forereef facies (Permian, west Texas and New Mexico): seepage reflux revisited. *Sedimentology* **49**, 1207–1227.

Middleburg J. (1989) A simple rate model for organic matter decomposition in marine sediments.pdf. *Geochim. Cosmochim. Acta* **53**, 1577–1581.

Mills J. V., DePaolo D. J. and Lammers L. N. (2021) The influence of Ca:CO3 stoichiometry on Ca isotope fractionation: Implications for process-based models of calcite growth. *Geochim. Cosmochim. Acta* **298**, 87–111.

Mruk D. H. (1989) Diagenesis of the Capitan Limestone, Upper Permian, McKittrick Canyon, West Texas. In *Subsurface and Outcrop Examination of the Capitan Shelf Margin, Northern Delaware Basin*. SEPM (Society for Sedimentary Geology), pp. 387–406.

Mucci A., Canuel R. and Zhong S. (1989) The solubility of calcite and aragonite in sulfate-free seawater and the seeded growth kinetics and composition of the precipitates at 25 °C. *Chem. Geol.* **74**, 309–320.

Murray S. T., Higgins J. A., Holmden C., Lu C. and Swart P. K. (2021) Geochemical fingerprints of dolomitization in Bahamian

carbonates: Evidence from sulphur, calcium, magnesium and clumped isotopes ed. C. Hollis. *Sedimentology* **68**, 1–29.

Mutti M. E. and Simo J. A. (1993) Stratigraphic patterns and cycle-related diagenesis of upper yates formation, Permian, Guadalupe Mountains. In *Carbonate Sequence Stratigraphy: Recent Developments and Applications* (eds. R. G. Loucks and J. F. Sarg). AAPG Memoir. The American Association of Petroleum Geologists, Tulsa, Oklahoma, pp. 515–534.

Mutti M. and Simo J. A. (1994) Distribution, petrography and geochemistry of early dolomite in cyclic shelf facies, yates formation (Guadalupian), Capitan Reef Complex, USA. In *Dolomites* (eds. B. Purser, M. Tucker and D. Zenger). Blackwell Publishing Ltd., Oxford, UK, pp. 91–107.

Ning M., Lang X., Huang K., Li C., Huang T., Yuan H., Xing C., Yang R. and Shen B. (2020) Towards understanding the origin of massive dolostones. *Earth Planet. Sci. Lett.* **545**, 116403.

Osleger D. A. (1998) Sequence architecture and sea-level dynamics of Upper Permian shelfal facies, Guadalupe Mountains, southern New Mexico. *J. Sediment. Res.* **68**, 327–346.

Paytan A. (2004) Seawater sulfur isotope fluctuations in the cretaceous. *Science* **304**, 1663–1665.

Paytan A., Kastner M., Campbell D. and Thiemens M. H. (1998) Sulfur isotopic composition of Cenozoic seawater sulfate. *Science (80-.)* **282**, 1459–1462.

Planavsky N. J., Bekker A., Hofmann A., Owens J. D. and Lyons T. W. (2012) Sulfur record of rising and falling marine oxygen and sulfate levels during the Lomagundi event. *Proc. Natl. Acad. Sci. U. S. A.* **109**, 18300–18305.

Present T. M., Adkins J. F. and Fischer W. W. (2020) Variability in sulfur isotope records of phanerozoic seawater sulfate. *Geophys. Res. Lett.* **47,** e2020GL088766.

Present T. M., Gutierrez M., Paris G., Kerans C., Grotzinger J. P. and Adkins J. F. (2019) Diagenetic controls on the isotopic composition of carbonate-associated sulphate in the Permian Capitan Reef Complex, West Texas ed. N. Tosca. *Sedimentology* **66**, 2605–2626.

Present T. M., Paris G., Burke A., Fischer W. W. and Adkins J. F. (2015) Large Carbonate Associated Sulfate isotopic variability between brachiopods, micrite, and other sedimentary components in Late Ordovician strata. *Earth Planet. Sci. Lett.* **432**, 187–198.

Razionale D., Bryant R. and Blättler C. (2021) Adapting automated instrumentation for high-throughput calcium isotope measurements by MC-ICP-MS. *Rapid Commun. Mass Spectrom.*, e9249.

Reddy M. M. and Nancollas G. H. (1976) The crystallization of calcium carbonate. IV. The effect of magnesium, strontium and sulfate ions. *J. Cryst. Growth* **35**, 33–38.

Rennie V. C. F., Paris G., Sessions A. L., Abramovich S., Turchyn A. V. and Adkins J. F. (2018) Cenozoic record of $\delta^{34}S$ in foraminiferal calcite implies an early Eocene shift to deep-ocean sulfide burial. *Nat. Geosci.* **11**, 761–765.

Rennie V. C. F. and Turchyn A. V. (2014) The preservation of δSSO434 and δOSO418 in carbonate-associated sulfate during marine diagenesis: A 25 Myr test case using marine sediments. *Earth Planet. Sci. Lett.* **395**, 13–23.

Richardson J. A., Keating C., Lepland A., Hints O., Bradley A. S. and Fike D. A. (2019a) Silurian records of carbon and sulfur cycling from Estonia: The importance of depositional environment on isotopic trends. *Earth Planet. Sci. Lett.* **512**, 71–82.

Richardson J. A., Newville M., Lanzirotti A., Webb S. M., Rose C. V., Catalano J. G. and Fike D. A. (2019b) Depositional and diagenetic constrains on the abundance and spatial variability of carbonate-associated sulfate. *Chem. Geol.* **523**, 59–72.

Ridgwell A. (2005) A mid mesozoic revolution in the regulation of ocean chemistry. *Mar. Geol.* **217**, 339–357.

Riechelmann S., Mavromatis V., Buhl D., Dietzel M., Hoffmann R., Jöns N., Kell-Duivestein I. and Immenhauser A. (2018) Echinoid skeletal carbonate as archive of past seawater magnesium isotope signatures – Potential and limitations. *Geochim. Cosmochim. Acta* **235**, 333–359.

Rivers J. M., Varghese L., Yousif R., Whitaker F. F., Skeat S. L. and Al-Shaikh I. (2019) The geochemistry of Qatar coastal waters and its impact on carbonate sediment chemistry and early marine diagenesis. *J. Sediment. Res.* **89**, 293–309.

Rivers J. M., Yousif R., Kaczmarek S. E. and Al-Shaikh I. (2021) Cenozoic coastal carbonate deposits of Qatar: Evidence for dolomite preservation bias in highly-arid systems. *Sedimentology* **68**, 771–787.

Rose C. V., Webb S. M., Newville M., Lanzirotti A., Richardson J. A., Tosca N. J., Catalano J. G., Bradley A. S. and Fike D. A. (2019) Insights into past ocean proxies from micron-scale mapping of sulfur species in carbonates. *Geology* **47**, 833–837.

Rush J. and Kerans C. (2010) Stratigraphic response across a structurally dynamic shelf: The latest guadalupian composite sequence at Walnut Canyon, New Mexico, U.S.A. *J. Sediment. Res.* **80**, 808–828.

Sarg J. F. (1981) Petrology of the Carbonate-evaporite Facies Transition of the Seven Rivers Formation (Guadalupian, Permian), Southeast New Mexico. *SEPM J. Sediment. Res.* **51**, 73–96.

Sarg J. F., Markello J. R. and Weber L. J. (1999) The second-order cycle, carbonate-platform growth, and reservoir, source, and trap prediction. In *Advances in Carbonate Sequence Stratigraphy*. SEPM (Society for Sedimentary Geology), pp. 11–34.

Schmidt V. (1977) Inorganic and organic reef growth and subsequent diagenesis in the Permian Capitan Reef Complex, Guadalupe Mountains, Texas, New Mexico. In *Upper Guadalupian Facies, Permian Reef Complex, Guadalupe Mountains, New Mexico and West Texas, 1977 Field Conference Guidebook* (eds. M. E. Hileman and S. J. Mazzullo). SEPM (Society for Sedimentary Geology), Midland, Texas, pp. 93–131.

Scholle P. A., Ulmer D. S. and Melim L. A. (1992) Late-stage calcites in the Permian Capitan Formation and its equivalents, Delaware Basin margin, west Texas and New Mexico: evidence for replacement of precursor evaporites. *Sedimentology* **39**, 207–234.

Schurr S. L., Strauss H., Mueller M. and Immenhauser A. (2021) Assessing the robustness of carbonate-associated sulfate during hydrothermal dolomitization of the Latemar platform, Italy. *Terra Nov.* **33**, 621–629.

Silver B. A. and Todd R. G. (1969) Permian Cyclic Strata, Northern Midland and Delaware Basins, West Texas and Southeastern New Mexico. *Am. Assoc. Pet. Geol. Bull.* **53**, 2223–2251.

Sjoberg E. L. (1978) Kinetics and mechanism of calcite dissolution in aqueous solutions at low temperatures. *Stock. Contrib. Geol.* **XXXII**, 1–92.

Smith B. P., Cantine M. D., Bergmann K. D., Ramos E. J., Martindale R. C. and Kerans C. (2021) Arid coastal carbonates and the phanerozoic record of carbonate chemistry. *AGU Adv.* **2**, e2021AV000386.

Smith B. P., Larson T., Martindale R. C. and Kerans C. (2020) Impacts of basin restriction on geochemistry and extinction patterns: A case from the Guadalupian Delaware Basin, USA. *Earth Planet. Sci. Lett.* **530**, 115876.

Staudigel P. T., Higgins J. A. and Swart P. K. (2021) An abrupt Middle-Miocene increase in fluid flow into the Leeward Margin

Great Bahama Bank, constraints from $\delta^{44}Ca$ and $\Delta 47$ values. *Earth Planet. Sci. Lett.* **553**, 116625.

Stiller M., Rounick J. S. and Shasha S. (1985) Extreme carbon-isotope enrichments in evaporating brines. *Nature* **316**, 434–435.

Tang J., Dietzel M., Böhm F., Köhler S. J. and Eisenhauer A. (2008) Sr^{2+}/Ca^{2+} and $^{44}Ca/^{40}Ca$ fractionation during inorganic calcite formation: II. Ca isotopes. *Geochim. Cosmochim. Acta* **72**, 3733–3745.

Thode H. G., Monster J. and Dunford H. B. (1961) Sulphur isotope geochemistry. *Geochim. Cosmochim. Acta* **25**, 159–174.

Tinker S. W. (1998) Shelf-to-basin facies distributions and sequence stratigraphy of a steep-rimmed carbonate margin; Capitan depositional system, McKittrick Canyon, New Mexico and Texas. *J. Sediment. Res.* **68**, 1146–1174.

Tyrrell, Jr, W. W. (1969) Criteria uuseful in interpreting environments of unlike but time-equivalent carbonate units (Tansill-Capitan-Lamar), Capitan Reef Complex, West Texas and New Mexico. In *Depositional Environments in Carbonate Rocks*. SEPM (Society for Sedimentary Geology), pp. 80–97.

Walter L. M. (1986) Relative efficiency of carbonate dissolution and precipitation during diagenesis: a progress report on the role of solution chemistry. In *Roles of Organic Matter in Sediment Diagenesis*. SEPM (Society for Sedimentary Geology), pp. 1–11.

Wang Z., Hu P., Gaetani G., Liu C., Saenger C., Cohen A. and Hart S. (2013) Experimental calibration of Mg isotope fractionation between aragonite and seawater. *Geochim. Cosmochim. Acta* **102**, 113–123.

Wilde G. L., Rudine S. F. and Lambert L. L. (1999) Formal designation: Reef trail member, bell Canyon formation, and its significance for recognition of the Guadalupian-Lopingian Boundary. In *Geologic Framework of the Capitan Reef*. SEPM (Society for Sedimentary Geology), pp. 63–83.

Wu Q., Ramezani J., Zhang H., Yuan D. xu, Erwin D. H., Henderson C. M., Lambert L. L., Zhang Y. chu and Shen S. zhon (2020) High-precision U-Pb zircon age constraints on the Guadalupian in West Texas, USA. *Palaeogeogr. Palaeoclimatol. Palaeoecol.* **548**, 109668.

Young E. D., Galy A. and Nagahara H. (2002) Kinetic and equilibrium mass-dependent isotope fractionation laws in nature and their geochemical and cosmochemical significance. *Geochim. Cosmochim. Acta* **66**, 1095–1104.

Yurewicz D. A. (1977) The origin of the massive facies of the lower and middle Capitan Limestone (Permian), Guadalupe Mountains, New Mexico and west Texas. In *Upper Guadalupian Facies, Permian Reef Complex, Guadalupe Mountains, New Mexico and West Texas, 1977 Field Conference Guidebook* (eds. M. E. Hileman and S. J. Mazzullo). SEPM (Society for Sedimentary Geology), Midland, Texas, pp. 45–92.

Associate editor: Adrian Immenhauser